Electro-chemo-mechanics Theory in Transfer Printing of Thin Films in

Electrolyte Solutions

Yue Zhang and Baoxing Xu*

Department of Mechanical and Aerospace Engineering, University of Virginia,

Charlottesville, VA, USA

Abstract: Transfer printing of thin films on an electrode substrate such as graphene on asgrown metal substrates in an electrolyte solution environment by applying an electrical field has provided a facile manufacturing technique to attain a precise delivery and assembly of thin film-based structures in a broad range of materials. The technique is underpinned by the electro-chemo-mechanical interfacial delamination, yet the fundamental theory is lacking. In the present study, we have established a comprehensive electro-chemo-mechanics theoretical framework of film detachment from various electrode substrates in an electrolyte solution environment. The bubble nucleation and subsequent kinetic growth due to the electrolysis of solution are first proposed and incorporated into the crack propagation of interface to predict the delamination of film from inert metal electrode substrates. Then, the film detachment induced by electrochemical etching to both interfacial bonds of film/electrode substrates and electrode substrates with chemically active metal materials is systematically investigated. The etching resultant kinetic model of bond breaking and failure is developed and also coupled with the bubble growth-induced interfacial delamination to describe their synergistic effect on the film detachment from electrode substrates with both types of electrode materials and polarity (i.e. anode or cathode). Afterward, we have implemented the electro-chemo-mechanics models into finite element method though a subroutine program. Computational results show remarkable agreement with theoretical predictions for both delamination mechanisms of solution electrolysis and electrochemical etching, regardless of materials of films, substrates and electrolyte solutions, and also are well confirmed with experimental results from literature in a good consistency. Further, a mechanical peeling force model equivalent has been developed to quantitatively estimate the electrochemical reaction-induced delamination and to discuss the application capacity of electrical field assistant transfer printing. The established

^{*} Corresponding author: <u>bx4c@virginia.edu</u>

electro-chemo-mechanics theory is expected to lay a foundation for quantitative understanding and controlling of transfer printing of thin films by the electrochemical field.

Keywords: electro-chemo-mechanics theory; transfer printing; interfacial delamination; bubble nucleation and growth; electrochemical etching.

1. Introduction

Transfer printing is a technology of picking up a material from a donor substrate and releasing it onto a receiver substrate with the help of an intermediate soft stamp (Carlson et al., 2012) and is the foundation in the manufacturing of almost an entire class of wearable technologies, in particular, film-based flexible electronics and devices (Fan et al., 2008; Jung et al., 2010; Nam et al., 2009; Wie et al., 2018; Yoon et al., 2015). From a mechanics point of view, transfer printing is a delamination process with a competing fracture path along the stamp/film interface or the film/substrate (donor or receiver) interface. A successful transfer requires the higher adhesion strength at the stamp/film interface than that at the film/donor interface, and once the stamp is peeled off, the delamination at the film/donor interface will occur, leading to the pickup of the film onto the stamp. In the subsequent printing step, a stronger adhesion strength at the film/receiver interface than that at the stamp/film interface is required to leave the film onto the receiver substrate when taking off the stamp. Over the past years, numerous assistant technologies are developed to improve the yield and control precision of the transfer printing technology by regulating these delamination competitions at interfaces. For example, applying a kinetic or shear loading to the stamp proves to modulate the adhesion strength due to the ratedependent viscoelastic properties of the soft stamp and has been utilized to control the transfer printing of thin films (Chen et al., 2013; Meitl et al., 2005). A series of environmental assistant approaches have also been developed to control the transfer printing by leveraging responses of interface delamination to external environment stimuli. For example, on the basis of the idea of the thermal mismatch between two different materials, thermal-assistant transfer printing is proposed, where the heating stimulus is introduced to initiate the separation of device components from the stamp (Tian et al., 2012) (Xu et al., 2016). Chemical etching is another popular means to help release films by chemically etching a well-designed sacrificial layer or the donor substrates and has been widely used in the transfer printing of 2D materials (Mahenderkar et al., 2017) (Yoon et al., 2010) and the deterministic assembly of multilayered structures and large-area flexible electronics (Hwang et al., 2014). Recently, an electrical field is applied to control the chemical reaction-induced delamination of interfaces, referred to as electrochemical transfer printing. This electrochemical reaction could lead to a highly controlled interfacial delamination by adjusting the applied voltage in a high accuracy and proves to be particularly powerful to detach a large-scale ultrathin film from electrode substrate (Gao et al., 2012; Lu et al., 2019; Zhang et al., 2018b).

To provide a quantitative guidance of these transfer printing technologies, several theoretical mechanics models have been proposed to describe interfacial delamination of films from substrates in dry air conditions by considering elasticity (Peng and Chen, 2015) and viscoelasticity of films (Afferrante and Carbone, 2016; Peng et al., 2014), heterogeneous structures (Xia et al., 2013) and micro-adhesive structures (Qian et al., 2017; Xue et al., 2015) of films, and interfacial friction/sliding (Begley et al., 2013; Yao et al., 2008) between films and substrates. For the transfer printing in a liquid environment, we have established theoretical models that are coupled with the physical capillary interaction (Park et al., 2021; Zhang et al., 2017b; Zhang et al., 2020) or the kinetic chemical reaction (Wie et al., 2018; Zhang et al., 2019) between liquid and solid materials and mechanical deformation of thin films. Similarly, in the electrochemical transfer printing, it is expected to be a synergistic process of interfacial delamination from breaks of interfacial bonds or etching of substrate, electrolysis of solution solvent such as water associated with bubble generation and growth, and mechanical deformation of films in an electrical field, but the underlying fundamental electro-chemomechanic theory is lacking. It should note that most of the existing work on electro-chemomechanics is primarily focused on the damage and fracture in bulk materials, such as the li-ion battery and electrode materials, and is incapable of describing detachment of films during the electrochemical transfer printing. For example, in the study of failure in electrode materials, the coupling of ion diffusion field with mechanical field in elastic solids is emphasized to obtain a modified J-integral and energy release rate (Gao and Zhou, 2013; Xu and Zhao, 2018; Zhang et al., 2017a). By contrast, in electrochemical transfer printing of films, the electrochemical

reaction could occur in the liquid solvent itself, such as the electrolysis of water (Mickle et al., 2019; Wang et al., 2011), where oxygen or hydrogen bubbles are generated at the interface of film/electrode substrates, and provide a driving force to delaminate the interface. Usually, this bubble generation-induced interfacial delamination is coupled with bonding breaks of interface by electrochemical etching (Cherian et al., 2015a), which is also beyond the capability of the existing electro-chemo-mechanics models. More importantly, ion diffusion into solid materials of both film and substrate during the electrochemical delamination process in transfer printing is not allowed because it will cause damages or containments to films or affect reusability of substrates. An electro-chemo-mechanics theoretical model that enables the description of detachment of films from substrate for the electrochemical transfer printing is needed.

In the present study, we have established a comprehensive electro-chemo-mechanics theory of film detachment from an electrode substrate in an electrolyte solution. The details of theoretical development of electro-chemo-mechanics model are presented in Section 2. First, the interface delamination driven by a bubble force from the solvent solution electrolysis is elucidated. A bubble nucleation and growth model is proposed and incorporated into the interface to predict the film detachment from inert metal substrates. After that, a kinetic etching model is developed to describe the interface delamination driven by electrochemical reaction between electrolyte and active metal materials of either substrates or interfacial bonds between substrate and film. Further, these mechanisms of interfacial delamination by the bubble growth and electrochemical etching are coupled through the superposition of crack propagation at interface. In Section 3, the finite element model is developed to simulate the interfacial delamination process between film and electrode substrates by implementing the electrochemo-mechanics models through the DISP subroutine program of finite element software package ABAQUS. Theoretical predictions, simulation calculations, and experimental results from literature are compared and discussed in Section 4. In Section 5, extended discussion on the capability of electrochemical delamination-driven transfer printing approach is given by proposing an equivalent mechanical peeling model. Concluding remarks are given in Section 6.

2. Theoretical framework

Fig. 1 (a) illustrates the concept of transferring a thin film by an electrochemical method. The electrochemical reaction cell consists of a pair of electrodes including a donor electrode substrate attached by a film (to be transferred) and a chemically inert plate as the counter electrode and an aqueous electrolyte solution. A direct current (DC) voltage ΔU is applied to the electrodes and will lead to detachment of the film from the donor electrode substrate. There are two electrochemical reaction-induced delamination mechanisms. The first one is the electrochemical reaction for the liquid itself, such as the electrolysis of water. Under an electrical voltage, oxygen or hydrogen gas bubbles near the interface of electrodes will be generated. The burst of these bubbles will provide a persistent force to break the interfacial adhesion between film and substrate, and leads to the interface delamination, as illustrated in Fig. 1 (b). For example, for a PMMA/graphene film on a copper (Cu) electrode substrate in an aqueous solution of K₂S₂O₈ electrolyte, under a voltage of 5V, hydrogen bubbles were generated at the graphene/Cu interfaces and led to the film detachment (Wang et al., 2011). The second mechanism is the electrochemical etching to electrode substrates or interfacial bonds between film and substrates. Fig. 1 (c) illustrates the electrochemical etching to interfacial bonds. This etching could break the interfacial adhesion between film and substrate and leads to an interface delamination. For example, for a PMMA/graphene film on a Cu₂O/Cu electrode substrate in an aqueous solution of NaCl electrolyte, the film delamination was observed under a voltage of 2.6V, and was caused by the electrochemical etching to the oxide layer of Cu₂O (Cherian et al., 2015a). Depending on the electrochemical reactions of electrodes in the electrolyte solutions, these two mechanisms of solution electrolysis and chemical etching could be coupled together and contribute to the delamination of films. We will show the establishment of their mechanics models below in detail.

2.1 Bubble transfer mechanics model

When the applied voltage could provide a minimum energy required to break the thermodynamics balance, as illustrated in Fig. 1 (b), the electrolysis of water will begin to generate oxygen gas at the anode and hydrogen gas at the cathode via

$$4 \rm{H}_2 \rm{O} + 4 e^- \leftrightarrow 2 \rm{H}_2 + 4 \rm{OH}^- \ (at \ cathode); \ and \ \ 2 \rm{H}_2 \rm{O} - 4 e^- \leftrightarrow \rm{O}_2 + 4 \rm{H}^+ (at \ anode) \ (1)$$

This kind of reaction usually occurs in neutral salt solutions such as NaCl solution (Liu et al., 2016), and the required minimum voltage is $\Delta U^0 = 1.23 \text{V}$ (Fisichella et al., 2014). When the solution is alkaline solution such as NaOH solution that helps increase electron transports in the electrochemical cell, the electrolysis of water will be conducted via $4\text{H}_2\text{O} + 4e^- \leftrightarrow 2\text{H}_2 + 40\text{H}^-$ (at cathode) and $40\text{H}^- - 4e^+ \leftrightarrow 0_2 + 2\text{H}_2\text{O}$ (at anode) (Peng and Wei, 2020). Note that an acid solution is usually not a good choice in the electrolysis of water because it will not only consume the electrode substrates but also increase the power loss in the reaction.

Once the gas generates near the electrodes, it will aggregate to a gas cluster after the dissolution of gas molecules reaches a supersaturation condition in the liquid solution, and the gas cluster will increase with the continuous generation of gas. Beyond a critical size, the cluster will nucleate into a stable gas bubble. Fig. 2 (a) illustrates the bubble nucleation and growth process, to determine the interfacial crack propagation process, in our model, we assumed that the bubbles would nucleate and distribute uniformly on the flat surface of substrate (Fisichella et al., 2014), and the produced gas in the reaction would diffuses equally into the bubbles. We should note that the bubbles could nucleate on specific sites such as the imperfections on the surface or pre-existing bubbles in practical applications (Brussieux et al., 2011). When the bubble nucleates at the interface, the nucleation theory needs to take into account the effect of both substrate surface and interfacial adhesion (Vachaparambil and Einarsrud, 2018). And therefore, the variation of the total energy in the nucleation process of the gas bubble can be obtained via:

$$\Delta G_{total} = \Delta G_{surface} + \Delta G_{bulk} + \Delta G^{0}_{crack}$$
 (2)

where $\Delta G_{surface}$ is the overall surface free energy of gas bubble, and assume the bubble is spherical, we have $\Delta G_{surface} = 2\pi r^2 (1 + cos(\pi - \theta))\gamma_{gl} + \pi r^2 (sin(\pi - \theta))^2 \gamma_{gl} cos(\pi - \theta)$ (Vachaparambil and Einarsrud, 2018). r is the radius of gas bubble, θ is the contact angle of gas bubble on the electrode substrate, γ_{gl} is the surface tension of gas bubble in liquid solution. ΔG_{bulk} is the bulk free energy of bubble and $\Delta G_{bulk} = \pi r^3 \frac{-(cos(\pi - \theta))^3 + 3cos(\pi - \theta) + 2}{3} \Delta G_v$. ΔG_v denotes the energy difference between the gaseous and dissolved states of the gas molecules in the bubble and thus is negative. ΔG_{crack}^0 is the

change of free energy due to the creation of new interfacial crack between film and substrate, where the film is assumed to be two-dimensional with uniform properties. This ΔG^0_{crack} represents the change of total adhesion energy at interface (Vlassak et al., 2005) and equals to the adhesion energy per unit area G_0 times the new area of crack. As shown in Fig. 2(a), the length of new crack by a single bubble in the propagation direction is the radius of bubble r, and the length in the width direction is the diameter of bubble 2r at $\theta > \frac{\pi}{2}$. Therefore we can have $\Delta G^0_{crack} = 2r^2G_0$. And the total energy in Equation (2) becomes:

$$\Delta G_{total} = 2\pi r^2 (1 + \cos(\pi - \theta)) \gamma_{gl} + \pi r^2 (\sin(\pi - \theta))^2 \gamma_{gl} \cos(\pi - \theta) + \pi$$

$$r^3 \frac{-(\cos(\pi - \theta))^3 + 3\cos(\pi - \theta) + 2}{3} \Delta G_v + 2r^2 G_0 = \pi (-(\cos(\pi - \theta))^3 + 3\cos(\pi - \theta) + 2)(r^2 \gamma_{gl} + \frac{r^3}{3} \Delta G_v) + 2r^2 G_0$$
(3)

Generally, both $\Delta G_{surface}$ and ΔG^0_{crack} increase with the increasing of the radius r of bubble, but ΔG_{bulk} decreases, as shown in Fig. 2 (b). As a result, ΔG_{total} shows a decrease after an initial increase to the maximum energy G_a at a critical radius r_0 . This non-monotonous variation suggests that the bubble growth is not an energy favorable process at $r < r_0$, where the associated gas cluster will be dissolved into the liquid; At $r > r_0$, the gas cluster gains a sufficient energy to overcome the energy barrier G_a and its continuous growth to a gas bubble becomes energetically favored. Take the first differentiation of ΔG_{total} with respect to r in Equation (3), we will have $\frac{d(\Delta G_{total})}{dr} = \pi(-(\cos(\pi - \theta))^3 + 3\cos(\pi - \theta) + 2)(2r\gamma_{gl} + r^2\Delta G_v) + 4rG_0$. And assume the gas bubble as a sphere with $\theta = \pi$, we will have $\frac{d(\Delta G_{total})}{dr} = 8\pi r \gamma_{gl} + 4\pi r^2\Delta G_v + 4rG_0$. Let $\frac{d(\Delta G_{total})}{dr} = 0$, we can obtain the nucleation radius r_0 :

$$r_0 = -\frac{2\pi\gamma_{gl} + G_0}{\pi\Delta G_v} \tag{4}$$

Substituting Equation (4) into Equation (3) with $\theta = \pi$, we have the maximum energy barrier G_a :

$$G_{a} = \frac{4\gamma_{gl}}{\pi} \left(\frac{2\pi\gamma_{gl} + G_{0}}{\Delta G_{v}}\right)^{2} - \frac{4\pi\Delta G_{v}}{3} \left(\frac{2\pi\gamma_{gl} + G_{0}}{\pi\Delta G_{v}}\right)^{3} + 2G_{0} \left(\frac{2\pi\gamma_{gl} + G_{0}}{\pi\Delta G_{v}}\right)^{2}$$
(5)

Fig. 2 (c) shows that both the maximum energy barrier G_a and critical radius r_0 increase with the increasing of the interfacial adhesion energy G_0 , suggesting a more difficult nucleation of the bubbles. We should note that at $G_0 = 0$, there is no interfacial delamination, and the nucleation energy in Equation (3) becomes $\Delta G_{total} = \pi(-(\cos(\pi-\theta))^3 + 3\cos(\pi-\theta) + 2)(r^2\gamma_{gl} + \frac{r^3}{3}\Delta G_v)$, and $\frac{d(\Delta G_{total})}{dr} = \pi(-(\cos(\pi-\theta))^3 + 3\cos(\pi-\theta) + 2)(2r\gamma_{gl} + r^2\Delta G_v)$. Therefore, the obtained nucleation radius will reduce to $r_0 = -\frac{2\gamma_{gl}}{\Delta G_v}$, which is independent on the contact angle and well consistent with that in the classical nucleation theory (Kelton and Greer, 2010).

After the nucleation, the gas bubble will grow because of the gas diffusion from the electrolyte solution. Assume a uniform distribution of gas in electrolyte, the gas concentration c_s is:

$$\frac{dc_s}{dt} = \frac{J_p}{V_s} - \frac{J_d}{V_s} \tag{6}$$

where V_s is the electrolyte volume, J_p is the gas production rate by the electrolysis of water and is a function of the current density I. $J_p = \frac{I}{nF_aN_b} = \frac{jS_r}{nF_aN_b}$, where j is the current density, S_r is the reaction area, N_b is the number of bubble distributed in the width of film, n is the number of electrons involved in the reaction, and F_a is the Faraday constant. J_a is the net gas flux rate into the bubble and can be related with the bubble growth via (Taqieddin, 2018):

$$J_d = \frac{dn_g}{dt} = 4\pi r^2 c_b \frac{dr}{dt} \tag{7}$$

where n_g is the amount of gas in the bubble, and c_b is the concentration of gas in the bubble. The difference of pressure between inside and outside the bubble is balanced by the surface tension of bubble, which gives $\Delta P = P_b - P_0 = \frac{2\gamma_{gl}}{r}$, where $P_b = c_b RT$ is the pressure inside the bubble, R is the universal gas constant and P_0 is the pressure in the solution, and we can have $c_b = \frac{P_0 r + 2\gamma_{gl}}{rRT}$. With Equation (7), Equation (6) can be rewritten as:

$$\frac{dc_S}{dt} = \frac{jS_r}{nF_aN_bV_S} - \frac{4\pi r(P_0r + 2\gamma_{gl})}{RTV_S} \frac{dr}{dt}$$
(8)

Equation (8) indicates that the bubble growth rate $\frac{dr}{dt}$ can be determined by the current density j in the reaction which is a function of the applied voltage ΔU (see **Appendix A**),

where the center of the bubble is assumed stationary during the process of bubble growth.

Further, the net gas diffusion rate J_d is the composition of the rate of the gas diffused into the bubble and the rate of the gas diffused out of the bubble. The diffusion rates of gas into and out of the bubble can be incorporated into their activation energy barriers (Kadyk et al., 2016). The activation energy for the gas diffusion across the surface of bubble with a radius r into the bubble is $\Delta G_{in} = \Delta G_{in}^{\infty} + (1 - \beta)(\Delta G_s + \Delta G_{cr})$, where ΔG_{in}^{∞} is the activation energy for the gas diffusion across an infinite large liquid-gas interface from liquid phase to gas phase, ΔG_s and ΔG_{cr} represent the free energy contribution from the increase of bubble surface area and interfacial crack area respectively. Similarly, the activation energy for the gas diffusion out of the bubble is $\Delta G_{out} = \Delta G_{out}^{\infty} - \beta(\Delta G_s + \Delta G_{cr})$, where ΔG_{out}^{∞} is the activation energy for the gas diffusion from gas phase to liquid phase, ΔG_s is the increase of bubble surface free energy per molar gas diffused into the bubble and ΔG_{cr} is the increase of energy due to the creation of a new interface crack per molar gas diffused into the bubble. In both ΔG_{in} and ΔG_{out} , β is a constant reflecting the asymmetry of the energy barrier and it is taken as 0.5. Therefore, the gas diffusion rate into the bubble is (Talapin et al., 2001):

$$J_{in} = 4\pi r^2 k_{in} c_s e^{\left(\frac{-(1-\beta)(\Delta G_s + \Delta G_{cr})}{RT}\right)}$$

$$\tag{9}$$

where $k_{in} = k_{in}^{0} e^{(\frac{-\Delta G_{in}^{\infty}}{RT})}$ is the gas transfer rate constant and c_s is the gas concentration in the solution. And the rate for gas diffused out of the bubble is

$$J_{out} = -4\pi r^2 k_{out} c_b e^{(\frac{\beta(\Delta G_S + \Delta G_{CT})}{RT})}$$
 (10)

where $k_{out} = k_{out}^{0} e^{\left(\frac{-\Delta G_{out}^{\infty}}{RT}\right)}$ is the gas dissolution rate constants, and the negative symbol denotes the direction of diffusion is out of the bubble. Therefore, the net gas diffusion rate is

$$J_d = J_{in} + J_{out} = 4\pi r^2 k_{in} c_s e^{\left(\frac{-(1-\beta)(\Delta G_S + \Delta G_{CT})}{RT}\right)} - 4\pi r^2 k_{out} c_b e^{\left(\frac{\beta(\Delta G_S + \Delta G_{CT})}{RT}\right)}$$
(11)

and the bubble growth rate is

$$\frac{dr}{dt} = \frac{J_d}{4\pi r^2 c_b} = k_{in} \frac{rRTc_s}{P_0 r + 2\gamma_{gl}} e^{\left(\frac{-(1-\beta)(\Delta G_S + \Delta G_{CT})}{RT}\right)} - k_{out} e^{\left(\frac{\beta(\Delta G_S + \Delta G_{CT})}{RT}\right)}$$
(12)

where $\frac{k_{out}}{k_{in}} = \frac{RT}{P_0} c_{sat}$, and c_{sat} is the saturation concentration of gas in electrolyte. During the bubble growth, the increase of bubble surface free energy per molar gas diffused into the bubble ΔG_S can be obtained using the Kevin equation and it is $\Delta G_S = \frac{2\gamma_{gl}}{rc_b} = \frac{2\gamma_{gl}RT}{P_0r + 2\gamma_{gl}}$.

Usually, a high quality transfer requires a negotiable mechanical deformation of films, which leads to much smaller mechanical deformation energy than that of the film/bubble interfacial energy, and the ΔG_{cr} can be simplified to $\Delta G_{cr} = \frac{G_cRT}{\pi(P_0r+2\gamma_{gl})}$ (Appendix B). Equation (12) becomes:

$$\frac{dr}{dt} = k_{in} \frac{r_{RTC_S}}{P_0 r + 2\gamma_{gl}} e^{(-(1-\beta)(\frac{2\gamma_{gl}}{P_0 r + 2\gamma_{gl}} + \frac{G_C}{\pi(P_0 r + 2\gamma_{gl})}))} - k_{out} e^{(\beta(\frac{2\gamma_{gl}}{P_0 r + 2\gamma_{gl}} + \frac{G_C}{\pi(P_0 r + 2\gamma_{gl})}))}$$
(13)

With the initial conditions $r(t=0)=r_0$ and $c_s(t=0)=0$, the bubble growth rate $\frac{dr}{dt}$ can be obtained by solving Equations (8) and (13). Besides, as the bubble nucleates at the interface, this Equation (13) takes into account the influence of interfacial adhesion on the bubble growth rate that usually cannot be achieved in the conventional analytical solution to the bubble growth in unbounded medium (Taqieddin et al., 2018). For example, its analysis shows the increase of interfacial adhesion energy G_c will lead to a decrease of bubble growth rate $\frac{dr}{dt}$, thus decreasing the interfacial delamination rate. In addition, when there is only bubble growth without interfacial crack propagation, the process can be modeled with the diffusion theory (Taqieddin et al., 2018; Vachaparambil and Einarsrud, 2020).

The growth of bubble will stop at a maximum radius r_{max} , and after that, the bubble will detach from the surface of substrate electrode and will not contribute to the interface delamination. Consider the force exerted on the bubble, we will have:

$$\sum F = F_s + F_b + F_{growth} + F_{cp} + F_d \tag{14}$$

where F is the vector of total force exerted on the bubble, which has components in the direction (x) perpendicular to the substrate surface and the direction (y) parallel to the substrate surface (**Appendix C**), F_s is the force of relevance to surface tension between bubble and

electrode surface, F_{growth} is the bubble growth force, F_b is the buoyancy force on the bubble, F_{cp} is the pressure force on the bubble in a contact with electrode surface, and F_d is the quasi-steady drag force due to the viscous fluid around the bubble. Assume a slow velocity of liquid near the bubble and a steady growth of bubble, the maximum radius of bubble growth r_{max} can be obtained from the balance of force (Appendix C), which is:

$$\sum F = -2\pi r_{max} \gamma_{gl} \sin^2(\pi - \theta) + \frac{4}{3}\pi r_{max}^3 (\rho_l - \rho_g) g + \pi r_{max} \sin^2(\pi - \theta) \frac{2\gamma_{gl}}{5} = 0$$
 (15)

where ρ_l is the density of liquid solution, ρ_g is the density of gas, g is the gravitational constant, and θ is the contact angle between bubble and surface of substrate. Therefore, the r_{max} can be written as:

$$r_{max} = \sqrt{\frac{6\gamma_{gl}\sin^2(\pi - \theta)}{5(\rho_l - \rho_g)g}}$$
 (16)

Here the coalescence of bubbles is neglected. This is because the number of existing bubbles each time is very small because of low gas generation rate under a small voltage, and the distance between adjacent bubbles could be much larger than the detach radius of bubble r_{max} . When the bubbles grow to the radius r_{max} , they will detach from the substrate and move to the solution before they are in contact with the adjacent bubbles. But we should note when the number of existing bubbles is large or the bubbles are distributed nonuniformly, there could be the substantial grow of bubbles due to coalescence (Brussieux et al., 2011). With the determination of r_{max} , the total time of bubble growth r_{growth} can be obtained from Equation (13) and it is

$$\int_0^{T_{growth}} \frac{dr}{dt} dt = \int_0^{T_{growth}} \left[k_{in} \frac{rRTc_s}{P_0r + 2\gamma_{gl}} e^{\left(-(1-\beta)\left(\frac{2\gamma_{gl}}{P_0r + 2\gamma_{gl}} + \frac{G_c}{\pi(P_0r + 2\gamma_{gl})}\right)\right)} \right. -$$

$$k_{out}e^{(\beta(\frac{2\gamma_{gl}}{P_0r+2\gamma_{gl}}+\frac{G_c}{\pi(P_0r+2\gamma_{gl})}))}]dt = (r_{max}-r_0) (17)$$

The interfacial crack propagation distance is $(r_{max} - r_0)$, and the averaged interfacial delamination rate driven by the bubble can be calculated via (Fisichella et al., 2014):

$$\overline{v_b} = \frac{r_{max} - r_0}{r_{growth}} \tag{18}$$

2.2 Electrochemical etching transfer mechanics model

Fig. 1 (c) shows schematic of the electrochemical etching to solid materials, where F and X denote the surface atoms of film and electrode substrate, respectively, S denotes the inner atom of electrode substrate, F – X is the interfacial bond of between film and electrode substrate, and X – S is the inner bond of electrode substrate. When the applied voltage ΔU is capable of providing a minimum energy required to break the thermodynamics balance, the electrochemical reaction will occur:

$$F - X - S + R + (-) ne^{-} \leftrightarrow F(P) + S - X(P)$$
 or (19)

$$F - X - S + R + (-)ne^{-} \leftrightarrow F - X(P) + S(P)$$
 (20)

where R denotes the reactant electrolyte (e.g. liquid and ions), P is the function groups of product, and n is the number of charge transfer in the reaction. Equation (19) implies the etching to the interface between film and electrode substrate, i.e. the breaking of the interfacial covalent bond F-X. For example, when a metal Ni film is on a SiO₂ substrate in an aqueous solution of alkaline electrolyte, the surface oxygen atoms of substrate and surface Ni atoms of film will form covalent interface bonds, and under an electrical voltage, the interface O-Ni bonds will break due to the reaction Ni-O-Si+H₂O+e⁻↔Ni+OH⁻+Si-OH, which leads to the detachment of Ni film (Wu et al., 2013). Note that when there is only liquid water without the applied electrical voltage or aqueous solution of alkaline electrolyte, the interfacial bonds could be broken by an applied mechanical loading with the help of hydrolysis reaction, and leads to the detachment of films, referred to as hydrolysis-driven transfer printing (Zhang et al., 2019). By contrast, Equation (20) indicates the etching to the electrode substrate, i.e. the breaking of inner bonds X-S. For example, when the electrode substrate of metal such as Cu and Ni is a cathode, the surface Cu atoms on the substrate bonded with film atoms will be etched away via the reaction F-Cu-Cu-2e⁻↔F+Cu²⁺+Cu (Shi et al., 2014). As a result, the film will be naturally separated from the electrode substrate. Besides, when the electrode substrate materials are metal oxides with a layer of oxygen atoms on the surface of substrate such as Cu₂O, the similar reactions will happen when the electrode substrate is used as an anode (Cherian et al., 2015a). For an instance, the surface oxygen atoms will be etched away through the reaction F-O-Cu+H₂O+2e⁻ ↔F+2OH-+Cu. As a result, the film originally bonded with these oxygen atoms will detach from the substrate, and in this case, the interfacial bond can be either covalent or noncovalent

bond. This electrochemical etching mechanism to substrates has been widely used to transfer graphene films that are on as-grown substrates by weak noncovalent interface bond such as vdW interactions (Shi et al., 2014). When the inner bonds X-S break, the surface atoms of substrate will dissolve into the solution as ions rather than staying on the films due to the weak interface vdW interactions. Therefore, the reaction of Equation (20) becomes $F - X - S + R + (-)ne^- \leftrightarrow F + X(P) + S(P)$. The electro-chemo-mechanics models will be developed below for these two different etching mechanisms.

When there is neither the applied chemical etchant nor electrical voltage, the reaction for the interface bond breaking is $F-X-S \leftrightarrow F + X-S$. In this reaction, the forward activation energy $\overrightarrow{G_r}$ is larger than the reverse activation energy $\overleftarrow{G_r}$, resulting in a smaller forward reaction rate than the reverse reaction rate, as illustrated in Fig. 3 (a). As a result, the net bond breaking rate is zero, and the interface will not delaminate. When there is a chemical etchant, the reaction becomes $F - X - S + R \leftrightarrow F + X(P) + S$, where the $\overrightarrow{G_f}$ becomes smaller than G_r , and the forward reaction rate is larger than that of the reverse reaction. Therefore, the interface will delaminate under this chemical etching. Furthermore, upon applying an electrical voltage ΔU , the reaction is $F - X - S + R + (-)ne^- \leftrightarrow F + X(P) +$ S(P). The $\overrightarrow{G_f}$ will decrease, and the $\overleftarrow{G_r}$ will increase, leading to an increased etching rate. Therefore, the interfacial delamination rate by electrochemical etching is larger than that of sole chemical etching. Specifically, when the film is on an anode substrate, we have the overall activation energy for the forward reaction $\overrightarrow{G_f} = \overrightarrow{G_{f0}} - \alpha n F_a E^a + \zeta G_c/N$, where $\overrightarrow{G_{f0}}$ is the intrinsic forward activation energy without ΔU . n is the number of electrons transfer in the reaction, F_a is the Faraday constant, E^a is the electrical potential at anode and depends on ΔU , and $\alpha n F_a E^a$ refects the contribution from the applied electrical potential. α is the charge transfer coefficient and it is taken as 0.5. N is the number of interfacial bond per unit area (i.e. number density of interfacial bonds), and the interfacial energy release rate $\Gamma_c = G_c$ when the deformation of film is neglected (Appendix B). $\zeta G_c/N$ represents the contribution from the interfacial fracture. The activation energy for the reverse reaction is $\overleftarrow{G_r} = \overleftarrow{G_{r0}} +$

 $(1-\alpha)nF_aE^a-(1-\zeta)G_c/N$, where $\overleftarrow{G_{r0}}$ is the intrinsic reverse activation energy, similar to $\overrightarrow{G_{f0}}$. The opposite sign of term nF_aE^a and G_c/N indicates that the effect of the electrical potential and interfacial adhesion on the energy barrier is completely opposite. With the increasing of G_c and deceasing of ΔU , the activation energy for the forward reaction increases, and the activation energy for the reverse reaction decreases, as shown in Fig. 3 (b). The electrical potential $E^a = E_0{}^a + \eta_{act}{}^a$, where $E_0{}^a$ is the equilibrium potential, and $\eta_{act}{}^a$ is the activation overpotential on the anode. Therefore, the current density at the anode can be obtained as

$$j = nF_a(c_f k_f e^{-\frac{-\alpha nF_a(E_0{}^a + \eta_{act}{}^a) + \zeta G_c/N}{RT}} - c_r k_r e^{-\frac{(1-\alpha)nF_a(E_0{}^a + \eta_{act}{}^a) - (1-\zeta)G_c/N}{RT}})$$
(21)

where c_f and c_r are the surface concentration of reactants and products, respectively. $k_f = A_f e^{-\frac{\overline{G_{f0}}}{RT}}$ and $k_r = A_r e^{-\frac{\overline{G_{r0}}}{RT}}$ are the rate constants for forward and reverse reactions, respectively, and A_f and A_r are constants. ζ is a constant reflecting the asymmetry of the interfacial adhesion energy term in the energy barrier and it's taken as 0.5 here. When the interface adhesion energy $G_c = 0$, the current density will be zero at the equilibrium potential $E_0{}^a$, and we can obtain the exchange current density $I_0 = nF_a c_f k_f e^{\frac{\alpha nF_a E_0{}^a}{RT}} = nF_a c_r k_r e^{\frac{-(1-\alpha)nF_a E_0{}^a}{RT}}$. And thus the current density in Equation (21) becomes:

$$j = j_0^a \left(e^{\frac{\alpha n F_a \eta_{act}^a - \frac{\zeta G_c}{N}}{RT}} - e^{\frac{-(1-\alpha)n F_a \eta_{act}^a + \frac{(1-\zeta)G_c}{N}}{RT}} \right)$$
 (22)

Similarly, when the film is on a cathode substrate, the current density in Equation (21) can also be obtained and it is:

$$j = -j_0{}^c \left(e^{\frac{\alpha n F_a \eta_{act}{}^c + \frac{\zeta G_c}{N}}{RT}} - e^{\frac{-(1-\alpha)n F_a \eta_{act}{}^c - \frac{(1-\zeta)G_c}{N}}{RT}} \right)$$
(23)

where $\eta_{act}{}^c$ is the activation overpotential on the cathode. With Equations (22) and (23), the relation between the current density j and applied voltage ΔU can be obtained (Appendix A), and the net interfacial bond breaking rate can be written as:

$$\omega = \frac{jS_r}{nF_a} = \frac{j_0{}^a S_r}{nF_a} \left(e^{\frac{\alpha nF_a \eta_{act} a - \frac{\zeta G_c}{N}}{RT}} - e^{\frac{-(1-\alpha)nF_a \eta_{act} a + \frac{(1-\zeta)G_c}{N}}{RT}} \right)$$
(24)

And the average interfacial delamination rate due to this electrochemical reaction is:

$$\overline{v_e} = \frac{1/N^{0.5}}{b_t N^{0.5}/\omega} = \frac{j_0{}^a S_r}{n F_a b_t N} \left(e^{\frac{\alpha n F_a \eta_{act} a_- \frac{\zeta G_c}{N}}{RT}} - e^{\frac{-(1-\alpha)n F_a \eta_{act} a_+ \frac{(1-\zeta)G_c}{N}}{RT}} \right)$$
(25)

where b_t is the width of film.

2.3 Coupling of bubble and electrochemical etching transfer models

Both the bubbles generation due to the electrolysis of water and electrochemical etching to solid bonds of electrode substrates or interface between film and electrode substrates may occur simultaneously in the electrochemical cell, and lead to an ultimate detachment of film. For example, a graphene film is delaminated from a Cu substrate with surface oxide layer Cu₂O, where Cu₂O/Cu substrate is used as a cathode, and NaCl solution is the electrolyte. Under an applied voltage ΔU , the delamination of the interface together with vigorous bubbles was observed, and the overall electrode reaction can be written as F-O-Cu+3H₂O+4e⁻↔F+4OH⁻ +Cu+H₂ (Cherian et al., 2015a). For the anodic reaction-induced delamination, a polymer film was observed to detach from a heavily doped Si substrate, where the Si substrate was the anode and the NaCl aqueous solution was electrolyte. The associated anodic reaction includes both the etching of Si substrate and generation of oxygen bubbles at interface: Si -8e-+8OH- \leftrightarrow H₂SiO₃+ 3H₂O + 2O₂ (Zhang et al., 2018a). In theory, when the applied voltage is smaller than the equilibrium potential of both electrochemical etching reaction ΔU_e^{0} and bubble generation reaction ΔU_h^0 , there will be no electrochemical reaction in the cell and the interface cannot be delaminated. When the applied voltage is larger than the equilibrium potential of $\Delta {U_e}^0$ but smaller than that of $\Delta {U_b}^0$, only the electrochemical etching reaction will be activated via Equation (20), and the interface delamination will be driven by the electrochemical etching of solid bonds near interface only. The resultant delamination rate will

be the same as Equation (25), i.e.
$$\overline{v} = \overline{v_e} = \frac{j_0^a S_r}{nF_a b_t N} \left(e^{\frac{\alpha n F_a \eta_{act}^a - \frac{\zeta G_c}{N}}{RT}} - e^{\frac{-(1-\alpha)nF_a \eta_{act}^a + \frac{(1-\zeta)G_c}{N}}{RT}} \right).$$

When the applied voltage is larger than both the equilibrium potential of $\Delta U_e^{\ 0}$ and $\Delta U_b^{\ 0}$, both the electrochemical etching reaction and bubble generation reaction will be activated, and

the reactions at the electrode of substrate and film are:

$$\begin{cases}
F - X - S + R + ne^{-} \leftrightarrow F + X(P) + S(P) \\
4H_{2}O + 4e^{-} \leftrightarrow 2H_{2} + 40H^{-}
\end{cases}$$
(cathode) or
$$\begin{cases}
F - X - S + R - ne^{-} \leftrightarrow F + X(P) + S(P) \\
2H_{2}O - 4e^{-} \leftrightarrow O_{2} + 4H^{+}
\end{cases}$$
(anode) (26)

And the overall reaction that leads to the interface delamination can be written as:

$$F - X - S + R + mH_2O + (n + m)e^- \leftrightarrow F + X(P) + S(P) + \frac{m}{2}H_2 + mOH^-$$
 (cathode) or
 $F - X - S + R + mH_2O - (n + 2m)e^- \leftrightarrow F + X(P) + S(P) + \frac{m}{2}O_2 + 2mH^+$ (anode) (27)

The electrochemical etching to electrode substrates or interfacial bonds between film and electrode substrates will leave gaps between the film and substrate, allowing the invasion of the electrolyte solution and gas bubbles into the film/substrate interface. The gas bubbles will produce a force that further facilitates the delamination process, as discussed in Section 2.1. Therefore, the interface delamination can be considered the superposition of the delamination by the electrochemical etching of solid bonds and the bubble force, and the overall delamination rate is:

$$\overline{v} = \overline{v_e} + \overline{v_b} = \frac{j_0{}^a S_r}{nF_a b_t N} \left(e^{\frac{\alpha nF_a \eta_{act} a - \frac{\zeta G_c}{N}}{RT}} - e^{\frac{-(1-\alpha)nF_a \eta_{act} a + \frac{(1-\zeta)G_c}{N}}{RT}} \right) + \frac{r_{max} - r_0}{T_{growth}}$$
(28)

3. Finite element (FE) modeling and simulations

We have implemented the electro-chemo-mechanics theory models of both bubble and electrochemical etching transfers and their coupling described in Sections 2 into the FE software ABAQUS/standard package to simulate the interfacial delamination between films and substrates. In FE simulations, films were modeled as elasticity, and electrode substrates were considered as a rigid material. The materials properties for films were Young's modulus E=2.9 GPa and Poisson ratio v=0.35 for PMMA film, and E=330 GPa and v=0.125 for MoS₂ (Wie et al., 2018). A 2D plane strain model was employed to simulate the interface fracture. The length of thin film was 1 cm, and the thickness varied from 10 nm to 1100 nm. The films were meshed with 4-node bi-linear plane strain elements. At least four layers of elements were used along the thickness in the thin film to well capture the through-thickness stress distribution and bending deformation. Mesh refinement with a high density in both film and substrate was

set near the interface, and mesh convergence was studied to confirm the discretization of model sufficiently enough for extracting converged interfacial crack growth rate. The interface interaction between film and substrate was described by a cohesive zone model (CZM). The critical energy release rate Γ_c was determined by the area under the curve of tractionseparation relation via $\Gamma_c = \sigma_0 \delta_c \int_0^1 \chi(\lambda) d\lambda$, where σ_0 is the maximum interface cohesive strength, and δ_c is critical crack tip separation. $\chi(\lambda)$ specifies the shape of the tractionseparation function with $\chi = \sigma/\sigma_0$ and $\lambda = \delta/\delta_c$, σ is the interface adhesive traction, and δ is the interface separation. When the interface energy release rate reaches the critical energy release rate Γ_c , the interfacial traction drops to zero, leading to a complete separation. The value of Γ_c will remain unchanged for the electrolysis of water reaction but will be updated for the electrochemical etching reaction. Besides, the trapezium shaped traction separation law was used in CZM, which has been widely used to model the interface delamination in elasticplastic peeling problems (Zhang et al., 2019). And the mixed-mode effects were neglected for the normal-separation dominant interface delamination process. To delaminate the interface in FE model, a loading was applied on the film with the loading rate u and loading angle ϕ . The loading rate is $u = \overline{v}(1 - \cos\phi)$ and has been programmed into the DISP subroutine, through which the interfacial interaction and electrochemical reaction are coupled together. Specifically, for bubble-driven delamination $u = \frac{r_{max} - r_0}{r_{growth}} (1 - cos\phi)$ obtained with the help of Equation

(18). For etching-driven delamination
$$u = \frac{j_0{}^a S_r}{nF_a b_t N} \left(e^{\frac{\alpha n F_a \eta_{act} a - \frac{\zeta G_c}{N}}{RT}} - \right)$$

 $e^{\frac{-(1-\alpha)nF_a\eta_{act}a_+\frac{(1-\zeta)G_c}{N}}{RT}}$ (1 - $\cos\phi$) obtained with the help of Equation (25). For delamination

driven by both bubble and etching
$$u = \left[\frac{j_0{}^a S_r}{nF_a b_t N} \left(e^{\frac{\alpha nF_a \eta_{act} a - \frac{\zeta G_c}{N}}{RT}} - e^{\frac{-(1-\alpha)nF_a \eta_{act} a + \frac{(1-\zeta)G_c}{N}}{RT}} \right) + \frac{1}{n} \left(e^{\frac{\alpha nF_a \eta_{act} a - \frac{\zeta G_c}{N}}{RT}} - e^{\frac{-(1-\alpha)nF_a \eta_{act} a + \frac{(1-\zeta)G_c}{N}}{RT}} \right) + \frac{1}{n} \left(e^{\frac{\alpha nF_a \eta_{act} a - \frac{\zeta G_c}{N}}{RT}} - e^{\frac{-(1-\alpha)nF_a \eta_{act} a + \frac{(1-\zeta)G_c}{N}}{RT}} \right) + \frac{1}{n} \left(e^{\frac{\alpha nF_a \eta_{act} a - \frac{\zeta G_c}{N}}{RT}} - e^{\frac{-(1-\alpha)nF_a \eta_{act} a + \frac{(1-\zeta)G_c}{N}}{RT}} \right) + \frac{1}{n} \left(e^{\frac{\alpha nF_a \eta_{act} a - \frac{\zeta G_c}{N}}{RT}} - e^{\frac{-(1-\alpha)nF_a \eta_{act} a + \frac{(1-\zeta)G_c}{N}}{RT}} \right) + \frac{1}{n} \left(e^{\frac{\alpha nF_a \eta_{act} a - \frac{\zeta G_c}{N}}{RT}} - e^{\frac{-(1-\alpha)nF_a \eta_{act} a + \frac{(1-\zeta)G_c}{N}}{RT}} \right) + \frac{1}{n} \left(e^{\frac{\alpha nF_a \eta_{act} a - \frac{\zeta G_c}{N}}{RT}} - e^{\frac{-(1-\alpha)nF_a \eta_{act} a + \frac{(1-\zeta)G_c}{N}}{RT}} \right) + \frac{1}{n} \left(e^{\frac{\alpha nF_a \eta_{act} a - \frac{\zeta G_c}{N}}{RT}} - e^{\frac{\alpha nF_a \eta_{act} a - \frac{\zeta G_c}{N}}{RT}} \right) + \frac{1}{n} \left(e^{\frac{\alpha nF_a \eta_{act} a - \frac{\zeta G_c}{N}}{RT}} - e^{\frac{\alpha nF_a \eta_{act} a - \frac{\zeta G_c}{N}}{RT}} \right) + \frac{1}{n} \left(e^{\frac{\alpha nF_a \eta_{act} a - \frac{\zeta G_c}{N}}{RT}} - e^{\frac{\alpha nF_a \eta_{act} a - \frac{\zeta G_c}{N}}{RT}} \right) + \frac{1}{n} \left(e^{\frac{\alpha nF_a \eta_{act} a - \frac{\zeta G_c}{N}} - e^{\frac{\alpha nF_a \eta_{act} a - \frac{\zeta G_c}{N}}{RT}} \right) + \frac{1}{n} \left(e^{\frac{\alpha nF_a \eta_{act} a - \frac{\zeta G_c}{N}} - e^{\frac{\alpha nF_a \eta_{act} a - \frac{\zeta G_c}{N}} - e^{\frac{\alpha nF_a \eta_{act} a - \frac{\zeta G_c}{N}}} \right) + \frac{1}{n} \left(e^{\frac{\alpha nF_a \eta_{act} a - \frac{\zeta G_c}{N}} - e^{\frac{\alpha nF_a \eta_{act} a - \frac{\zeta G_c}{N}}} \right) + \frac{1}{n} \left(e^{\frac{\alpha nF_a \eta_{act} a - \frac{\zeta G_c}{N}} - e^{\frac{\alpha nF_a \eta_{act} a - \frac{\zeta G_c}{N}}} \right) + \frac{1}{n} \left(e^{\frac{\alpha nF_a \eta_{act} a - \frac{\zeta G_c}{N}} - e^{\frac{\alpha nF_a \eta_{act} a - \zeta G_c}{N}} \right) + \frac{1}{n} \left(e^{\frac{\alpha nF_a \eta_{act} a - \zeta G_c}{N}} - e^{\frac{\alpha nF_a \eta_{act} a - \zeta G_c}{N}} \right) + \frac{1}{n} \left(e^{\frac{\alpha nF_a \eta_{act} a - \zeta G_c}{N}} - e^{\frac{\alpha nF_a \eta_{act} a - \zeta G_c}{N}} \right) + \frac{1}{n} \left(e^{\frac{\alpha nF_a \eta_{act} a - \zeta G_c}{N}} \right) + \frac{1}{n} \left(e^{\frac{\alpha nF_a \eta_{act} a - \zeta G_c}{N}} \right) + \frac{1}{n} \left(e^{\frac{\alpha nF_a \eta_{act} a - \zeta G_c}{N}} \right) + \frac{1}{n} \left(e^{\frac{\alpha nF_a \eta_{act} a - \zeta G_c}{N}} \right) + \frac{1}{n} \left(e^{\frac{\alpha nF_a \eta_{act}$$

 $\frac{r_{max}-r_0}{T_{growth}}](1-cos\phi)$ obtained with the help of Equation (28). The average crack propagation rate at the interface will be calculated via $\bar{v} = \frac{\Delta d}{\Delta T_d}$, where Δd is the overall interfacial crack propagation distance, and ΔT_d is the overall crack propagation time.

4. Results

With the average interfacial delamination rate $\overline{v_b} = 0$, we can calculate the quantitative relation between interfacial adhesion energy G_c and corresponding critical electrical voltage required to delaminate the interface ΔU_c for the bubble transfer through Equations (18) and (A.1-A.5). Fig. 4 (a) shows the theoretical calculations of ΔU_c versus G_c under different electrolyte solution concentrations C. The G_c shows an initial quick increase with the increasing of the ΔU_c . Afterward it increases slowly with an arrival of an eventual plateau with a maximum magnitude. The larger G_c indicates the requirement of higher ΔU_c that enables to delaminate the interface during the transfer printing, while the arrival of the plateau of the G_c indicates the maximum interface adhesion strength which the bubble force cannot overcome and the associated transfer printing process cannot deliver the films. Besides, when G_c is small, the effect of C can be neglected. In particular, when G_c is close to 0, ΔU_c represents the equilibrium potential of the reaction of electrolysis of water, which is independent of the electrolyte concentration C. By contrast, for a very larger G_c , it increases with the increasing of the C, suggesting that the increasing of C should facilitate the interface delamination. Further, Fig. 4 (a) shows that for the chemical covalent bonding interactions with $G_c < 4 \text{J/m}^2$, or vdW interactions with $G_c < 1.5 \text{J/m}^2$, such as the adhesion energy between graphene and Cu substrate (Xin et al., 2017), the bubble-driven force is fully capable of enabling delamination the interface for a successful transfer. Once the applied voltage ΔU is beyond the critical voltage ΔU_c , the interface will be delaminated. Fig. 4 (b) shows the interfacial delamination rate $\overline{v_b}$ as a function of ΔU , where G_c is taken 0.7J/m^2 in Equation (13), and the other parameters used in the theory are given in **Table 1**. Similar to that G_c , $\overline{v_b}$ arrives at a maximum magnitude $\overline{v_b}_{max} = 0.32 \, \text{mm/s}$ after an initial increase with the increasing of ΔU . With the increasing of ΔU , the current density in the electrochemical cell will reach the current density limit j_{lim} as analyzed in Equations A.4 and A.5. As a result, the maximum gas generation and bubble growth rates in Equation (8) will be obtained, which leads to $\overline{v_b}_{max}$. Fig. 4 (b) also shows that, at the beginning, the delamination rate increases with the increasing of the C, as the higher C will improve the current density in the cell and enhances the bubble generation rate. However, for different C, the delamination rate will finally come to

the same maximum rate limit, which agrees with the assumption in the theory that the j_{lim} is independent of the C. These theoretical variations agree well with parallel FE simulations and also are confirmed by literature experimental data with remarkable agreement (Fisichella et al., 2014). In addition, the ΔU (= ΔU_c) at $\overline{v_b} = 0$ is almost independent of the C when the adhesion energy G_c is small enough, which shows good agreement with that in Fig. 4(a).

Fig. 4 (c) shows the effect of the film's bending stiffness B, electrode substrate materials, and electrode polarity on the delamination rate $\overline{v_b}$, where the popular electrode materials of Au and Cu are taken as examples in calculations. When the substrate is used at cathode, the $\overline{v_h}$ increases when the electrode substrate materials change from Cu to the Au, because the corresponding interfacial adhesion energy between film and substrate decreases from G_c =0.7J/m² to G_c =0.25J/m² (Megra and Suk, 2019). When the substrate electrode changes from cathode to anode, for the Cu substrate material, the electrochemical etching reaction will occur rather than the electrolysis of water reaction because of the active chemical property of Cu, and thus Cu substrate cannot be used as anode in the bubble-driven transfer. By contrast, for the Au substrate, the electrolysis of water reaction will occur at anode instead of the etching reaction because of its inert chemical property. As a result, when the Au substrate is used as anode, a lower $\overline{v_b}$ is obtained than that as a cathode for the same applied voltage, because the generation rate of oxygen is lower than that of hydrogen in the same cell as shown in Equation (1), which leads to a lower bubble generation rate. Further, the $\overline{v_b}$ is nearly unchanged when the stiffness of film B increases from $B=4\times 10^{-8} N\cdot nm$ that corresponds to a single layer graphene to $B=2 N\cdot nm$ that corresponds to a PMMA film with 1 micron thickness regardless of electrode materials and electrode polarity, suggesting their deformation energy can be neglected compared to the interfacial adhesion energy in the bubble transfer. In the practical situation, coating a polymer film (typically with thickness about hundreds nanometers or several micrometers) on 2D materials will not change the interfacial delamination rate in the transfer process. In addition, these dependences of $\overline{v_b}$ are well confirmed with parallel FE simulations and also show good agreement with experiments measurements (Fisichella et al., 2014). By taking Cu as a typical noble metal electrode at cathode, we further calculate the $\overline{v_b}$. Fig. 4 (d) shows the theoretical calculations of the $\overline{v_b}$ as a function of electrolyte solution

concentration C for different types of electrolyte solution. The $\overline{v_b}$ increases with the increasing of C once the $\Delta U > \Delta U_c$. Besides, at C=0, the $\overline{v_b}$ equals to 0 because of zero current where the solution is not conductive and there is no bubble generated. The $\overline{v_b}$ will reach a constant with the increasing of C when the current density in the cell comes to the limit. In addition, the $\overline{v_b}$ shows a decrease when the solution changes from basic KOH solution to the (NH₄)S₂O₈ solution and to the neutral NaCl solution because of the decreased conductivity of ions, which results in a lower bubble generation rate. As shown in Fig. 4 (d) and **Table 2**, the remarkable agreement of these theoretical calculations with FE simulations and experimental data from reference (Fisichella et al., 2014) under the same operating conditions further validates the theoretical model of bubble transfer.

Similarly, for the electrochemical etching-driven interfacial delamination, the minimum electrical voltage required to delaminate the interface ΔU_c can also be obtained by solving Equation (25) with $\overline{v_e} = 0$. Fig. 5 (a) shows the theoretical calculations of the relation between ΔU_c and interfacial adhesion energy G_c . Similar to that of bubble force-induced interface delamination, the G_c increases with the increasing of the ΔU_c . It also shows that this relation is independent of the electrolyte concentration C, which is consistent with Equation (25), where at $G_c=0$, the ΔU_c is the equilibrium potential of the electrochemical etching reaction. In this delamination, the G_c can be far larger than the vdW force interactions of $1.5 \mathrm{J/m^2}$ between film and electrode substrates and will not limit its applications, and can also be used in transfer printing of film/electrode substrate systems with covalent bonds when the ΔU_c is larger than 0.6V. With Equation (25) and G_c =0.7J/m², consider Cu substrate as the anode in a (NH₄)S₂O₈ solution, Fig. 5 (b) shows the etching-driven interface delamination rate $\bar{v_e}$ as a function of applied voltage under different electrolyte concentrations C. The $\overline{v_e}$ increases with the increasing of ΔU_c and arrives at a maximum magnitude $\overline{v_e}_{max} = 0.03 \, \text{mm/s}$ due to the current density limit j_{lim} in the electrochemical cell. In addition, with the increasing of the C, the $\overline{v_e}$ increases, and while the ΔU_c required to start the delamination is the same for different C, which is consistent with the results in Fig. 5 (a). Although higher C requires a smaller voltage to reaching the maximum delamination rate, the ultimate delamination rate will

reach the same maximum rate limit because of the j_{lim} that is independent with the C. Most importantly, all these theoretical predictions show remarkable agreement with FE simulations and literature experiments (Shi et al., 2014).

To investigate the effect of mechanical deformation of film and selections of substrate materials on the delamination rate, Fig. 5 (c) shows the \bar{v}_e as a function of applied electrical voltage ΔU with the variation of the bending stiffness B of film and interfacial adhesion energy G_c . The $\overline{v_e}$ decreases when the G_c increases from G_c =0.7J/m² to G_c =3J/m². The critical electrical voltage ΔU_c also shows an increase with the increasing of G_c , consistent well with Fig. 5 (a). When the B increases from $B=2\times 10^{-4} N\cdot nm$ that corresponds to MoS₂ layers with 10 nm thickness to $B=2N\cdot nm$ that corresponds to a PMMA film with 1 micron thickness, the $\overline{v_e}$ remains approximately the same regardless of interfacial adhesion energy. This nearly unchanged $\overline{v_e}$ suggests that the mechanical deformation energy could be neglected in comparison with the interfacial adhesion energy in the etching-driven transfer. These theoretical predictions of $\overline{v_e}$ are well confirmed with parallel FE simulations and also show good agreement with experimental measurements. In addition, because of G_c independence on the current density limit j_{lim} , the maximum delamination rate $\overline{v_e}_{max}$ is also independent of G_c . Fig. 5 (d) shows the $\overline{v_e}$ versus ΔU when the substrate changes to cathode from anode. Note that an oxide layer is required on the surface of Cu substrate when it is used as cathode, and the etching of the oxygen atoms at the interface will lead to the delamination. The comparison shows that the critical voltage required to start the delamination is larger on cathode than that on anode because the minimum voltage required for the etching of Cu₂O reaction is larger than that of the etching of Cu reaction. However, the $\,\overline{v}_{e}\,$ can be larger on cathode than that on anode because the number density of O atoms is smaller than the number density of Cu atoms at the interface. Therefore, the total etching time of the oxide layer is smaller than the etching time of the surface Cu atoms. Similar to that in Fig. 4 (d), the NaCl solution leads to a lower $\overline{\nu_e}$ than that of the (NH₄)S₂O₈ solution with the same concentration because of a higher conductivity of the solution. Similarly, when the NaCl solution concentration increases from 0.1M to 0.5M, a higher $\overline{v_e}$ is also obtained. More importantly,

the experimental data from the literature (Cherian et al., 2015a) show great agreement with the theoretical results (Table 2) and confirm the mechanics model of chemical etching mechanism.

Further, Figs 4 and 5 show that the voltage required for the chemical etching-induced delamination is much lower than that of bubble force-driven delamination. For example, the voltage required for the etching of Cu reaction is 0.34V, while it is 1.23 V for electrolysis of water reaction. Besides, the delamination rate $\overline{v_e}$ is almost one order of magnitude smaller than that of bubble force-driven delamination $\overline{v_b}$. For chemically active substrate materials like Cu, the etching-driven and bubble-driven transfers can both work. And in the etching-driven transfer, the Cu needs to be treated as anode; By contrast, in the bubble-driven transfer, the Cu needs to be treated as cathode. However, for the chemically inert substrate materials such as Pt and Au, only the bubble-driven transfer can be used because these materials can hardly be etched.

Fig. 6 (a) summaries the comparison of the interfacial delamination rate \bar{v} enabled by both bubble (purple curve) and electrochemical etching (pink curve) mechanisms with $G_c = 0.7 \text{J/m}^2$ in Equation (28). Upon an increase of voltage, the \bar{v} quickly arrives at the maximum magnitude for electrochemical etching, while the bubble-driven delamination requires a higher voltage to the arrival of maximum \bar{v} yet with a higher maximum value. When the ΔU is larger than the critical voltages for activating both bubble generation and chemical etching, these both mechanisms will happen simultaneously during the interface delamination, as indicated by Equation (27). The resultant \bar{v} shows a rapid increases at the beginning, and then becomes slower when the delamination rate contributed by etching arrives at a constant. And eventually, it will also reach to a constant when the delamination rate contributed by bubble arrives at the maximum. Those results show great agreement with our FE simulations and literature experiments (Cherian et al., 2015a). Fig. 6 (b) further compares the \bar{v} by both bubble and etching mechanisms under different electrolyte concentration C. It suggests that the chemical etching should be the dominant mechanism at a small ΔU with $\overline{v_e} > \overline{v_b}$ (pink part in the curves). With the increase of ΔU , the bubble-induced delamination will exceed the contribution by etching with $\overline{v_e} < \overline{v_b}$, and will become the dominant mechanism to delaminate the interface (blue part in the curves). It also shows that with the increasing of C, the bubble force requires a higher voltage to become dominant. For both mechanisms, the critical voltage required to initiate the delamination at $\bar{v} = 0$ is nearly independent of C, well consistent with the results in Figs 4 and 5.

5. Discussion

To quantitatively understand the driving force that enables the interfacial delamination by the electrochemical reactions, **Fig. 7 (a)** illustrates an equivalent mechanical peeling model, where the film is peeled from a substrate in a dry air condition by a pure mechanical force and the delamination rate \bar{v} is assumed to be the same with that of the electrochemical method. With the principle of energy balance at a steady state delamination (Zhang et al., 2019), the equivalent mechanical peeling force can be obtained via $P_e = G_0 + 2NkTsinh^{-1}\left(\frac{v_c}{2(kT/h)l_{bond}e^{\left(\frac{E_a^*}{kT}\right)}}\right)$ for a 90 degree peeling, where P_e is the equivalent peeling force per unit width of film, v_c is the interfacial crack propagation rate, h is the Planck's constant, l_{bond} is the bond length at interface and E_a^* is the activation energy for bond breaking. For the coupled mechanism of bubble force and chemical etching-induced delamination, we have:

$$P_{e} = G_{0} + 2NkT sinh^{-1} \left(\frac{\bar{v}}{2(kT/h) l_{bond} e^{\left(-\frac{E_{a}^{*}}{kT} \right)}} \right)$$
(29)

Where the interfacial crack propagation rate is $\bar{v} = \frac{j_0{}^a S_r}{nF_a b_t N} \left(e^{\frac{\alpha nF_a \eta_{act} a - \frac{\zeta G_c}{N}}{RT}} - \frac{\zeta G_c}{N} \right)$

$$e^{\frac{-(1-\alpha)nF_a\eta_{act}^a + \frac{(1-\zeta)G_c}{N}}{RT}} + \frac{r_{max} - r_0}{T_{growth}} \text{ from Equation (28)}.$$

For simplification, when the interface delamination is driven only by bubble force, $P_e =$

$$G_0 + 2NkT sinh^{-1} \left(\frac{\overline{v_b}}{2(kT/h)l_{bond}e^{\left(-\frac{E_a^*}{kT}\right)}} \right)$$
, where $\overline{v_b} = \frac{r_{max} - r_0}{T_{growth}}$ from Equation (18); for the

interface delamination driven only by electrochemical etching mechanism, $P_e = G_0 + G_0$

$$2NkT sinh^{-1}\left(\frac{\overline{v_e}}{\frac{1}{2(kT/h)l_{bond}e}\left(-\frac{E_a^*}{kT}\right)}\right) \qquad , \qquad \text{where} \qquad \overline{v_e} = \frac{j_0{}^aS_r}{nF_ab_tN}\left(e^{\frac{\alpha nF_a\eta_{act}a_-\frac{\zeta G_c}{N}}{RT}} - \frac{1}{2(kT/h)l_{bond}e}\left(-\frac{E_a^*}{kT}\right)\right)$$

$$e^{\frac{-(1-\alpha)nF_a\eta_{act}a_+\frac{(1-\zeta)G_c}{N}}{RT}}$$
 from Equation (25). **Fig. 7 (b)** shows that the P_e by both mechanisms

increases with the increasing of ΔU till to a maximum of ~1.5N/m for a Cu electrode substrate. Besides, the P_e for only bubble-induced delamination mechanism is larger than that of the electrochemical etching mechanism, but lower than that of their coupled mechanism, which is in a good consistency with the results in Fig. 6a. The maximum P_e implies the capability that the electrochemical transfer can achieve. For example, when the interfacial strength is beyond this maximum value, the electrochemical reaction cannot induce a fully detachment of film from substrate in the transfer printing process and an external force should be applied to assist it.

6. Conclusion

In this work, we have developed a comprehensive electro-chemo-mechanics theory for transfer printing of films from various electrode substrates in an electrolyte solution environment. In this theory, the delamination mechanisms by both the bubble nucleation and growth due to the electrolysis of water and the electrochemical etching of solid bonds are proposed and coupled together to predict the interfacial delamination rate of the film detachment from electrode substrates. In particular, in the development of the bubble force-induced interfacial delamination model, the kinetic nucleation and growth of bubbles are elucidated by considering both the diffusion and dissolution of gas molecules in the electrolyte solution and are also theoretically formulated as a function of the applied electrical voltage and solution concentration. The theoretical analysis shows the bubble generation will increase once the applied electrical voltage is beyond a critical value but will arrive at a maximum value, leading to a maximum interfacial delamination rate. For the electrochemical etching mechanism, the etching to both the materials of electrode substrate itself and the interfacial bonds between film and electrode substrate are taken into account. Electrode materials and consideration of them as cathode or anode, and selection of electrolyte solutions and their concentration are investigated to clarify their effect on the applied critical electrical voltage and interfacial

delamination rate. A diagram is summarized to compare the dominative role of bubble force and electrochemical etching-induced delamination mechanisms and to guide the choice of film/electrode substrate materials, the applied electrical voltage, and the solution concentration for applications in in transfer printing. We have also developed a computational model to study the interfacial delamination with the help of cohesive zone model (CZM) by implementing the electro-chemo-mechanics theory model into finite element (FE) analysis. The predicted detachment rate of film by the electro-chemo-mechanics theory is incorporated into the FE model by programming the delamination into the DISP subroutine. The simulation results show remarkable agreement with theoretical predictions and literature experimental measurements for a wide variety of materials and electrode voltage. In addition, an equivalent mechanical peeling force is proposed to quantitatively estimate the peeling force that can be provided by electrochemical delamination. The maximum equivalent peeling force per unit width of film from Cu substrate (~1.5 N/m) as an example is obtained, suggesting the maximum adhesion strength capability of film/substrate systems that can be transferred by the electrochemical transfer printing in applications. This work lays a theoretical foundation for the quantitative understanding of interfacial delamination in film/electrode substrate systems, and will guide the immediate applications for controlling the electrical field assistant transfer printing of thin films in an electrolyte solution with a great accuracy.

Acknowledgments: This work is supported by NSF CMMI-1728149 and NSF-CMMI-1928788.

Appendix A. The relation between the current density j and the applied voltage ΔU

Equation (8) shows that the bubble growth rate depends on the current density j in the electrochemical cell, and can be determined by the applied electrical voltage ΔU . The ΔU should equal to the sum of reversible equilibrium potential and overpotentials (η) (Angulo et al., 2020) which is:

$$\Delta U = \Delta U^{0} + \sum \eta = \Delta U^{0} + \eta_{act}{}^{a} - \eta_{act}{}^{c} + \eta_{ohm} + \eta_{con}{}^{a} - \eta_{con}{}^{c}$$
 (A.1)

where ΔU^0 is the reversible equilibrium potential and represents the minimum thermal dynamic energy required for the reaction. $\eta_{act}{}^a$ and $\eta_{act}{}^c$ are the activation overpotentials on the anode and cathode, respectively. The relation between current density and activation overpotential can be obtained by the Butler-Volmer equation (Bard and Faulkner, 2001):

$$j = j_0^a \left(e^{\left(\frac{\alpha n F_a \eta_{act}^a}{RT}\right)} - e^{\left(\frac{-(1-\alpha)n F_a \eta_{act}^a}{RT}\right)}\right) \text{ (anode), and } j = -j_0^c \left(e^{\left(\frac{\alpha n F_a \eta_{act}^c}{RT}\right)} - e^{\left(\frac{-(1-\alpha)n F_a \eta_{act}^c}{RT}\right)}\right) \text{ (cathode)(A.2)}$$

where j_0 is the exchange current density. η_{ohm} is the ohmic overpotential and denotes the potential loss due to the resistance in the electrochemical cell. This resistance contains two parts, one is the electrical resistance to flow of current in the electrical components like circuit and electrodes; and the other resistance is the ionic component related to the transport of ions through the electrolyte solution. The relation between ohmic overpotential and current density can be obtained by the Ohm's law (Chen et al., 2017):

$$\eta_{ohm} = j(R_{ele} + R_{con}) = jR_{ele} + j\frac{d_e}{\chi} = jR_{ele} + j\frac{d_e}{c\sum_i \lambda_i z_i}$$
 (A.3)

where R_{ele} is the electrical resistance in the electrical component and R_{con} is the ionic resistance of the electrolyte solution. The ionic resistance $R_{con} = \frac{d_e}{\chi} = \frac{d_e}{c \sum_i \lambda_i z_i}$, in which d_e is the distance between two electrodes and χ is the conductivity of electrolyte solution. λ_i is the molar conductivity of the ion i, z_i is number of charges of ion i, and C is the concentration of ions. Here in order to obtain the analytical solution for the relation between voltage and current, we made the following assumptions. First, given a low gas generation rate under small voltage, we assume the number of generated bubbles each time is very small. This assumption is in fact consistent with the preference in most electrochemical transfer experiments as the large number of bubbles will cause the severe deformation and damage in

the transferred thin films. Second, the bubbles would escape once they detach from the electrode substrates and did not affect the electrical resistance in the electrochemical cell. But we should note that when the bubbles on the electrode and in the solution become significant, they will change the effective electrical resistance in the electrochemical cell, which will need complicated numerical calculations to solve the relation between voltage and current (Vachaparambil and Einarsrud, 2021; Zhao et al., 2019). $\eta_{con}{}^a$ and $\eta_{con}{}^c$ are the concentration overpotentials on the anode and cathode, respectively, which is the potential loss in the buildup of reactant concentration gradient from the electrolyte to the electrode surface due to the mass transport speed limits near the surface of electrodes at high currents. The relation between concentration overpotentials and current density can be written as (Murthy et al., 2018):

$$\eta_{con}{}^{a} = -\frac{{}^{2RT}}{{}^{nF_a}}\ln(1 - \frac{j}{j_{lim}{}^{a}}) \tag{A.4}$$

$$\eta_{con}{}^{c} = \frac{2RT}{nF_a} \ln(1 - \frac{j}{j_{lim}{}^{c}}) \tag{A.5}$$

where $j_{lim}{}^a$ and $j_{lim}{}^c$ are the current density limits on the anode and cathode, respectively. At last, Equations (A.1-A.5) can be used to describe the relation between applied electrical voltage ΔU and current density j.

Appendix B. Theoretical analysis of energies associated with mechanical bending deformation of film and interfacial crack

In the delamination driven by bubble force, the interface crack propagates along the *x*-direction due to the bubble growth, and the resultant increase of bending deformation energy in film is (Harvey et al., 2017):

$$U_b = \frac{1}{2} \int_0^r \frac{2rEt^3}{12} \left(\frac{d^2w}{dx^2}\right)^2 dx = \frac{\pi^4 E t^3 A^2}{96r^2}$$
 (B.1)

where $w(x) = \frac{A}{2} \left[1 + \cos(\frac{\pi x}{r}) \right]$ is the deflection of film, A is the magnitude of film deflection, E is the elastic modulus of film, and t is film thickness. The in-plane elastic strain energy is:

$$U_s = 2r^2t\left(\frac{E}{2}(\varepsilon^R)^2\right) = \frac{\pi^4 E t A^4}{256r^2}$$
 (B.2)

where $\varepsilon^R = \frac{1}{2r} \int_0^r (\frac{dw}{dx})^2 dx = \frac{\pi^2 A^2}{16r^2}$ is the averaged axial relaxation strain. And the increasing of interfacial energy is $U_c = 2r^2 G_c$, where G_c is the interfacial adhesion energy per unit area. Therefore the increasing of total energy due to the interface crack propagation is:

$$U_t = \frac{\pi^4 E t^3 A^2}{96r^2} + \frac{\pi^4 E t A^4}{256r^2} + 2r^2 G_c$$
 (B.3)

The increasing of total energy per molar gas diffused into bubble is:

$$\Delta G_{cr} = \frac{\delta(U_t)}{\delta n_q} = -\frac{\pi^3 E t^3 A^2}{192 r^5 c_b} - \frac{\pi^3 E t^3 A^4}{512 r^5 c_b} + \frac{G_c R T}{\pi (P_0 r + 2\gamma_{ql})}$$
(B.4)

As shown in **Fig. B1** (a), when the film is soft, it will be deformed and wrapped around bubble by the force between film and surface of bubble. When the film is hard, it cannot be deformed and will not be in contact with the surface of bubble. The deformation of film is the result of competition between film deformation energy and film/bubble interfacial energy. The change of total energy is:

$$\Delta E_t = Lb_t \left(\frac{B}{24r^2}\right) + Lb_t \gamma_{gl} \left(cos\theta_{fl} - 1\right) = Lb_t \left(\frac{Et^3}{24r^2}\right) + Lb_t \gamma_{gl} \left(cos\theta_{fl} - 1\right) \ (B.5)$$

where θ_{fl} is the contact angle between film and liquid, L is the film length and b_t is the film width and $B = Et^3$ is the bending stiffness of film. As shown in Fig. B1 (a), when $\Delta E_t = Lb_t\left(\frac{Et^3}{24r^2}\right) + Lb_t\gamma_{gl}(\cos\theta_{fl}-1) > 0$, it indicates that the magnitude of film deformation energy is larger than the interfacial energy, and the interfacial energy is not large enough to deform the film. For example, when the film is single layer graphene on a 1 micron thick

PMMA layer, the deformation of film can be neglected. In practical experiments of transferring graphene, PMMA layer can be used to reduce the deformation in graphene and to improve the quality of transferred graphene film. When the deformation of film can be neglected, the energy contributed by interfacial crack ΔG_{cr} can be simplified and written as:

$$\Delta G_{cr} = \frac{G_c RT}{\pi (P_0 r + 2\gamma_{gl})} \tag{B.6}$$

In the delamination driven by electrochemical etching, the deformation of film at the interfacial crack tip is the result of competition between film deformation energy and film/liquid interfacial energy. The variation of the energy is:

$$\Delta E_t = \frac{1}{2} \left(\frac{b_t B}{4L^3} \right) H^2 - L b_t \gamma_{gl} cos\theta_{fl} = \frac{b_t E t^3 H^2}{8L^3} - L b_t \gamma_{gl} cos\theta_{fl}$$
 (B.7)

where H is the crack tip opening. The interfacial energy release rate in the crack propagation is $\Gamma_c = \frac{1}{2} \left(\frac{B}{4L^4} \right) H^2 + G_c$. As shown in **Fig. B1** (b), when $\frac{b_t E t^3 H^2}{8L^3} < L b_t \gamma_{gl} cos \theta_{fl}$, the deformation energy in the film can be neglected compared to the interfacial energy. The interfacial energy release rate can be simplified to $\Gamma_c = G_c$. For example, when the film is MoS₂ layers, the deformation of film can be neglected compared to the interfacial energy (Ma et al., 2017).

Appendix C. Force analysis on bubble on the surface of substrate electrode

During the bubble growth, the total force exerted on the bubble can be written as(Chen et al., 2012):

$$\sum F_x = F_{s,x} + F_{arowth,x} + F_{b,x} + F_{cp} \tag{C.1}$$

$$\sum F_y = F_{s,y} + F_{growth,y} + F_{b,y} + F_d \tag{C.2}$$

where x-direction is perpendicular to the surface of substrate, and y-direction is parallel to the surface of substrate. F_s is the force of relevance to surface tension between bubble and substrate surface, F_{growth} is the bubble growth force, F_b is the buoyancy force on the bubble, F_{cp} is the pressure force on the bubble in a contact with substrate surface, and F_d is the quasi-steady drag force due to the viscous fluid around the bubble. The surface tension force between bubble and substrate surface $F_{s,x}$ and $F_{s,y}$ can be obtained via:

$$F_{s,x} = -2r_f \gamma_{gl} \frac{\pi}{\theta_a - \theta_r} [\cos(\theta_a) - \cos(\theta_r)], \text{ and } F_{s,y} = -2.5r_f \gamma_{gl} \frac{\pi(\theta_a - \theta_r)}{\pi^2 - (\theta_a - \theta_r)^2} [\sin(\theta_a) + \sin(\theta_r)]$$
(C.3)

where $r_f = rsin(\pi - \theta)$ is the contact radius between bubble and solid surface, and θ_a and θ_r are the advancing contact angle and receding contact angle of bubble on solid surface, respectively. The force due to the unsteady growth of bubble can be written as:

$$F_{growth,x} = -\rho_l \pi r^2 (r\ddot{r} + \frac{3\dot{r}^2}{2})\cos(\theta_i), \text{ and } F_{growth,y} = -\rho_l \pi r^2 (r\ddot{r} + \frac{3\dot{r}^2}{2})\sin(\theta_i)$$
(C.4)

where ρ_l is the density of liquid solution, and θ_l is the angle between x-direction and the direction of growth force. The buoyancy force from liquid on the bubble can be written as:

$$F_{b,x} = \frac{4}{3}\pi r^3 (\rho_l - \rho_g) \boldsymbol{g} \cdot \boldsymbol{e}_x \text{ and } F_{b,y} = \frac{4}{3}\pi r^3 (\rho_l - \rho_g) \boldsymbol{g} \cdot \boldsymbol{e}_y$$
 (C.5)

where ρ_g is the density of gas, g is the gravity vector, and e_x and e_y are the direction vector of x-direction and y-direction, respectively. The contact pressure force on the bubble is only in x-direction, which results from the overpressure inside the bubble and is a function of the pressure difference across the bubble interface. It can be expressed as:

$$F_{cp} = \pi r_f^2 \frac{2\gamma_{gl}}{r_s} \tag{C.6}$$

where $r_s = 5r$ is the equivalent radius at the bubble top. The quasi-steady drag force due to the viscous fluid flowing around the bubble is only in y-direction, which can be written as:

$$F_d = 3C_d \pi \mu_l^2 Re_b \tag{C.7}$$

where C_d is the quasi-steady drag coefficient, and μ_l is the liquid bulk dynamic viscosity. Re_b is the bubble Reynolds number and can be given by $Re_b = \frac{2r\rho_l u_r}{\mu_l}$, where u_r is the relative velocity between the bubble center of mass and the liquid bulk velocity.

When the x-direction is parallel to the direction of gravity, where the surface of substrate is perpendicular to the gravity, and the portion of surface tension force in the y-direction becomes zero, the surface tension force can be simplified to $F_s = -2\pi r_f \gamma_{gl} \sin(\pi - \theta) = -2\pi r \gamma_{gl} \sin^2(\pi - \theta)$, where θ is the contact angle between bubble and surface of substrate. The portion of buoyancy force in the y-direction also becomes zero and the buoyance force can be simplified as $F_b = \frac{4}{3}\pi r^3(\rho_l - \rho_g)g$.

In the electrochemical system, the velocity of liquid near the bubble is low, and therefore the drag force from the viscous fluid on the bubble F_d can be neglected compared to the surface tension force and buoyance force. In addition, the bubble growth can be regarded as steady growth in the electrolysis of water and as a result, the force due to the unsteady growth of bubble F_{growth} can also be neglected. Therefore, the sum of force exerted on the bubble can be simplified to $\sum F = F_s + F_b + F_{cp} = -2\pi r \gamma_{gl} \sin^2(\pi - \theta) + \frac{4}{3}\pi r^3 (\rho_l - \rho_g)g + \pi r \sin^2(\pi - \theta) \frac{2\gamma_{gl}}{5}$. The maximum radius of bubble growth r_{max} can be obtained from the balance of force, which is:

$$\sum F = -2\pi r_{max} \gamma_{gl} \sin^2(\pi - \theta) + \frac{4}{3}\pi r_{max}^3 (\rho_l - \rho_g) g + \pi r_{max} \sin^2(\pi - \theta) \frac{2\gamma_{gl}}{5} = 0 \text{ (C.8)}$$

Reference:

Afferrante, L., Carbone, G., 2016. The ultratough peeling of elastic tapes from viscoelastic substrates. Journal of the Mechanics and Physics of Solids 96, 223-234.

Angulo, A., van der Linde, P., Gardeniers, H., Modestino, M., Rivas, D.F., 2020. Influence of bubbles on the energy conversion efficiency of electrochemical reactors. Joule 4, 555-579.

Bard, A.J., Faulkner, L.R., 2001. Fundamentals and applications. Electrochemical Methods 2, 580-632.

Begley, M.R., Collino, R.R., Israelachvili, J.N., McMeeking, R.M., 2013. Peeling of a tape with large deformations and frictional sliding. Journal of the Mechanics and Physics of Solids 61, 1265-1279.

Brussieux, C., Viers, P., Roustan, H., Rakib, M., 2011. Controlled electrochemical gas bubble release from electrodes entirely and partially covered with hydrophobic materials. Electrochimica Acta 56, 7194-7201.

Carlson, A., Bowen, A.M., Huang, Y., Nuzzo, R.G., Rogers, J.A., 2012. Transfer printing techniques for materials assembly and micro/nanodevice fabrication. Advanced Materials 24, 5284-5318.

Chen, D., Pan, L.-m., Ren, S., 2012. Prediction of bubble detachment diameter in flow boiling based on force analysis. Nuclear engineering and design 243, 263-271.

Chen, H., Feng, X., Huang, Y., Huang, Y., Rogers, J.A., 2013. Experiments and viscoelastic analysis of peel test with patterned strips for applications to transfer printing. J. Mech. Phys. Solids 61, 1737-1752.

Chen, Y., Mojica, F., Li, G., Chuang, P.Y.A., 2017. Experimental study and analytical modeling of an alkaline water electrolysis cell. International Journal of Energy Research 41, 2365-2373. Cherian, C.T., Giustiniano, F., Martin-Fernandez, I., Andersen, H., Balakrishnan, J., Ozyilmaz, B., 2015a. 'Bubble-free' electrochemical delamination of CVD graphene films. Small 11, 189-194.

Cherian, C.T., Giustiniano, F., Martin-Fernandez, I., Andersen, H., Balakrishnan, J., Özyilmaz, B., 2015b. 'Bubble-Free'electrochemical delamination of CVD graphene films. Small 11, 189-194.

Fan, Z., Ho, J.C., Jacobson, Z.A., Razavi, H., Javey, A., 2008. Large-scale, heterogeneous integration of nanowire arrays for image sensor circuitry. Proceedings of the National Academy of Sciences 105, 11066-11070.

Fisichella, G., Di Franco, S., Roccaforte, F., Ravesi, S., Giannazzo, F., 2014. Microscopic mechanisms of graphene electrolytic delamination from metal substrates. Applied Physics Letters 104, 233105.

Gao, L., Ren, W., Xu, H., Jin, L., Wang, Z., Ma, T., Ma, L.P., Zhang, Z., Fu, Q., Peng, L.M., Bao, X., Cheng, H.M., 2012. Repeated growth and bubbling transfer of graphene with millimetre-size single-crystal grains using platinum. Nature communications 3, 699.

Gao, Y., Zhou, M., 2013. Coupled mechano-diffusional driving forces for fracture in electrode materials. Journal of Power Sources 230, 176-193.

Harvey, C.M., Wang, B., Wang, S., 2017. Spallation of thin films driven by pockets of energy concentration. Theoretical and Applied Fracture Mechanics 92, 1-12.

Huo, J., 2004. Electrochemical planarization of copper for microelectronic applications. OGI School of Science & Engineering at OHSU.

- Hwang, S.W., Song, J.K., Huang, X., Cheng, H., Kang, S.K., Kim, B.H., Kim, J.H., Yu, S., Huang, Y., Rogers, J.A., 2014. High-Performance Biodegradable/Transient Electronics on Biodegradable Polymers. Advanced Materials 26, 3905-3911.
- Jung, I., Shin, G., Malyarchuk, V., Ha, J.S., Rogers, J.A., 2010. Paraboloid electronic eye cameras using deformable arrays of photodetectors in hexagonal mesh layouts. Applied Physics Letters 96, 021110.
- Kadyk, T., Bruce, D., Eikerling, M., 2016. How to enhance gas removal from porous electrodes? Scientific reports 6, 1-14.
- Kelton, K.F., Greer, A.L., 2010. Nucleation in condensed matter: applications in materials and biology. Elsevier.
- Liu, L., Liu, X., Zhan, Z., Guo, W., Xu, C., Deng, J., Chakarov, D., Hyldgaard, P., Schröder, E., Yurgens, A., 2016. A Mechanism for Highly Efficient Electrochemical Bubbling Delamination of CVD-Grown Graphene from Metal Substrates. Advanced Materials Interfaces 3, 1500492.
- Lu, W., Cheng, S., Yan, M., Wang, Y., Xia, Y., 2019. Selective soluble polymer–assisted electrochemical delamination of chemical vapor deposition graphene. Journal of Solid State Electrochemistry 23, 943-951.
- Ma, X., Liu, Q., Xu, D., Zhu, Y., Kim, S., Cui, Y., Zhong, L., Liu, M., 2017. Capillary-Force-Assisted Clean-Stamp Transfer of Two-Dimensional Materials. Nano letters 17, 6961-6967.
- Mahenderkar, N.K., Chen, Q., Liu, Y.-C., Duchild, A.R., Hofheins, S., Chason, E., Switzer, J.A., 2017. Epitaxial lift-off of electrodeposited single-crystal gold foils for flexible electronics. Science 355, 1203-1206.
- Megra, Y.T., Suk, J.W., 2019. Adhesion properties of 2D materials. Journal of Physics D: Applied Physics 52, 364002.
- Meitl, M.A., Zhu, Z.-T., Kumar, V., Lee, K.J., Feng, X., Huang, Y.Y., Adesida, I., Nuzzo, R.G., Rogers, J.A., 2005. Transfer printing by kinetic control of adhesion to an elastomeric stamp. Nature Materials 5, 33-38.
- Mickle, A.D., Won, S.M., Noh, K.N., Yoon, J., Meacham, K.W., Xue, Y., McIlvried, L.A., Copits, B.A., Samineni, V.K., Crawford, K.E., 2019. A wireless closed-loop system for optogenetic peripheral neuromodulation. Nature 565, 361.
- Murthy, S.K., Sharma, A.K., Choo, C., Birgersson, E., 2018. Analysis of concentration overpotential in an all-vanadium redox flow battery. Journal of The Electrochemical Society 165, A1746.
- Nam, S., Jiang, X., Xiong, Q., Ham, D., Lieber, C.M., 2009. Vertically integrated, three-dimensional nanowire complementary metal-oxide-semiconductor circuits. Proceedings of the National Academy of Sciences 106, 21035-21038.
- Park, J.K., Zhang, Y., Xu, B., Kim, S., 2021. Pattern transfer of large-scale thin membranes with controllable self-delamination interface for integrated functional systems. Nature communications 12, 1-10.
- Peng, L., Wei, Z., 2020. Catalyst engineering for electrochemical energy conversion from water to water: water electrolysis and the hydrogen fuel cell. Engineering 6, 653-679.
- Peng, Z., Chen, S., 2015. Effect of bending stiffness on the peeling behavior of an elastic thin film on a rigid substrate. Physical Review E 91, 042401.
- Peng, Z., Wang, C., Chen, L., Chen, S., 2014. Peeling behavior of a viscoelastic thin-film on a

rigid substrate. International Journal of Solids and Structures 51, 4596-4603.

Qian, J., Lin, J., Xu, G.-K., Lin, Y., Gao, H., 2017. Thermally assisted peeling of an elastic strip in adhesion with a substrate via molecular bonds. Journal of the Mechanics and Physics of Solids 101, 197-208.

Shi, L., Liu, Y., Yang, F., Gao, L., Sun, J., 2014. A symmetrical bi-electrode electrochemical technique for high-efficiency transfer of CVD-grown graphene. Nanotechnology 25, 145704.

Talapin, D.V., Rogach, A.L., Haase, M., Weller, H., 2001. Evolution of an ensemble of nanoparticles in a colloidal solution: theoretical study. The Journal of Physical Chemistry B 105, 12278-12285.

Taqieddin, A., 2018. Modeling of Bubbles Hydrodynamics and Mass Transfer in Electrochemical Gas-Evolving Systems. Northeastern University.

Taqieddin, A., Allshouse, M.R., Alshawabkeh, A.N., 2018. Critical Review—Mathematical formulations of electrochemically gas-evolving systems. Journal of The Electrochemical Society 165, E694.

Tian, B., Liu, J., Dvir, T., Jin, L., Tsui, J.H., Qing, Q., Suo, Z., Langer, R., Kohane, D.S., Lieber, C.M., 2012. Macroporous nanowire nanoelectronic scaffolds for synthetic tissues. Nature materials 11, 986.

Vachaparambil, K.J., Einarsrud, K.E., 2018. Explanation of bubble nucleation mechanisms: a gradient theory approach. Journal of The Electrochemical Society 165, E504.

Vachaparambil, K.J., Einarsrud, K.E., 2020. Modeling interfacial mass transfer driven bubble growth in supersaturated solutions. AIP Advances 10, 105024.

Vachaparambil, K.J., Einarsrud, K.E., 2021. Numerical simulation of continuum scale electrochemical hydrogen bubble evolution. Applied Mathematical Modelling 98, 343-377.

Vlassak, J.J., Lin, Y., Tsui, T.Y., 2005. Fracture of organosilicate glass thin films: environmental effects. Materials Science and Engineering: A 391, 159-174.

Wang, Y., Zheng, Y., Xu, X., Dubuisson, E., Bao, Q., Lu, J., Loh, K.P., 2011. Electrochemical delamination of CVD-grown graphene film: toward the recyclable use of copper catalyst. ACS nano 5, 9927-9933.

Widodo, C.S., Sela, H., Santosa, D.R., 2018. The effect of NaCl concentration on the ionic NaCl solutions electrical impedance value using electrochemical impedance spectroscopy methods, AIP Conference Proceedings. AIP Publishing LLC, p. 050003.

Wie, D.S., Zhang, Y., Kim, M.K., Kim, B., Park, S., Kim, Y.-J., Irazoqui, P.P., Zheng, X., Xu, B., Lee, C.H., 2018. Wafer-recyclable, environment-friendly transfer printing for large-scale thin-film nanoelectronics. Proceedings of the National Academy of Sciences 115, E7236-E7244.

Wu, L.-K., Hu, J.-M., Zhang, J.-Q., Cao, C.-N., 2013. A silica co-electrodeposition route to highly active Ni-based film electrodes. Journal of Materials Chemistry A 1, 12885-12892.

Xia, S., Ponson, L., Ravichandran, G., Bhattacharya, K., 2013. Adhesion of heterogeneous thin films—I: Elastic heterogeneity. Journal of the Mechanics and Physics of Solids 61, 838-851.

Xin, H., Borduin, R., Jiang, W., Liechti, K.M., Li, W., 2017. Adhesion energy of as-grown graphene on copper foil with a blister test. Carbon 123, 243-249.

Xu, B., Akhtar, A., Liu, Y., Chen, H., Yeo, W.H., Park, S.I., Boyce, B., Kim, H., Yu, J., Lai, H.Y., 2016. An epidermal stimulation and sensing platform for sensorimotor prosthetic control, management of lower back exertion, and electrical muscle activation. Advanced Materials 28,

4462-4471.

Xu, R., Zhao, K., 2018. Corrosive fracture of electrodes in Li-ion batteries. Journal of the Mechanics and Physics of Solids 121, 258-280.

Xue, Y., Zhang, Y., Feng, X., Kim, S., Rogers, J.A., Huang, Y., 2015. A theoretical model of reversible adhesion in shape memory surface relief structures and its application in transfer printing. Journal of the Mechanics and Physics of Solids 77, 27-42.

Yao, H., Della Rocca, G., Guduru, P., Gao, H., 2008. Adhesion and sliding response of a biologically inspired fibrillar surface: experimental observations. Journal of The Royal Society Interface 5, 723-733.

Yoon, J., Jo, S., Chun, I., Jung, I., Kim, H., Meitl, M., Menard, E., Li, X., Coleman, J., Paik, U., Rogers, J., 2010. GaAs photovoltaics and optoelectronics using releasable multilayer epitaxial assemblies. Nature 465, 329-U380.

Yoon, J., Lee, S.M., Kang, D., Meitl, M.A., Bower, C.A., Rogers, J.A., 2015. Heterogeneously integrated optoelectronic devices enabled by micro-transfer printing. Advanced Optical Materials 3, 1313-1335.

Zhang, H., Liu, Y., Yang, C., Xiang, L., Hu, Y., Peng, L.M., 2018a. Wafer-Scale Fabrication of Ultrathin Flexible Electronic Systems via Capillary-Assisted Electrochemical Delamination. Advanced materials 30, e1805408.

Zhang, H., Liu, Y., Yang, C., Xiang, L., Hu, Y., Peng, L.M., 2018b. Wafer-scale fabrication of ultrathin flexible electronic systems via capillary-assisted electrochemical delamination. Advanced Materials 30, 1805408.

Zhang, M., Qu, J., Rice, J.R., 2017a. Path independent integrals in equilibrium electro-chemoelasticity. Journal of the Mechanics and Physics of Solids 107, 525-541.

Zhang, Y., Kim, B., Gao, Y., Wie, D.S., Lee, C.H., Xu, B., 2019. Chemomechanics of transfer printing of thin films in a liquid environment. International Journal of Solids and Structures 180, 30-44.

Zhang, Y., Liu, Q., Xu, B., 2017b. Liquid-assisted, etching-free, mechanical peeling of 2D materials. Extreme Mechanics Letters 16, 33-40.

Zhang, Y., Yin, M., Baek, Y., Lee, K., Zangari, G., Cai, L., Xu, B., 2020. Capillary transfer of soft films. Proceedings of the National Academy of Sciences 117, 5210-5216.

Zhao, X., Ren, H., Luo, L., 2019. Gas bubbles in electrochemical gas evolution reactions. Langmuir 35, 5392-5408.

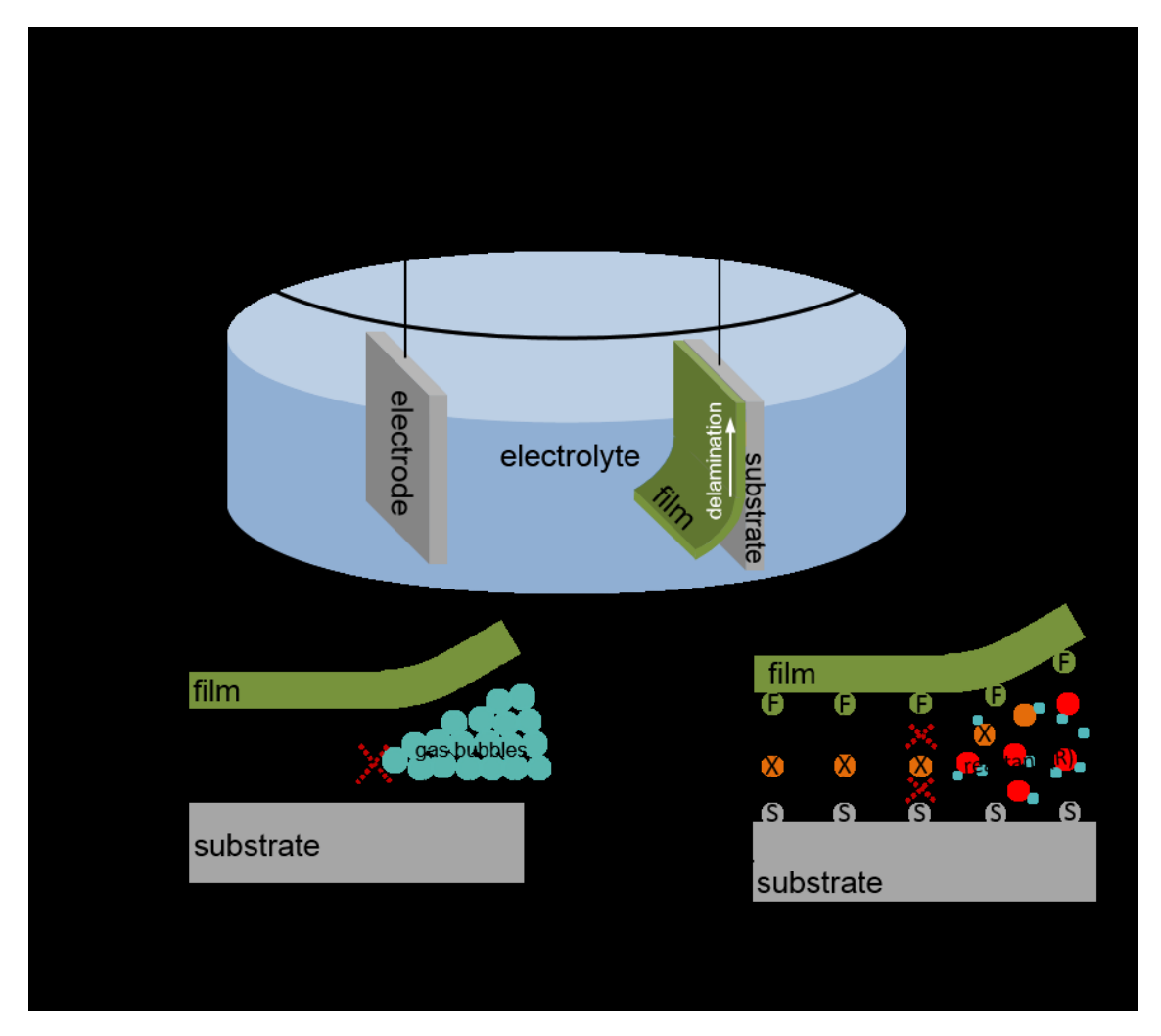


Fig. 1. Electro-chemo-mechanics mechanism in transfer of thin film on an electrode substrate. (a) Schematic illustration of thin film delamination from an electrode substrate in an electrolyte solution under an applied electrical voltage ΔU . (b) Interface delamination between film and substrate enabled by the force of bubbles which are generated from the electrolysis of water reaction via $4H_2O + 4e^- \leftrightarrow 2H_2 + 4OH^-$ (cathode), or $2H_2O 4e^- \leftrightarrow 0_2 + 4H^+$ (anode). The wavy curves between film and electrode substrate denote their interaction of either non-covalent or covalent bonds, and the hollow spheres in light blue illustrate the generated hydrogen or oxygen gas bubbles that break the interfacial bonds. (c) Interface delamination between film and substrate driven by electrochemical etching to solid bonds via $F - X - S + R + (-)ne^- \leftrightarrow F(P) + S - X(P)$ (1) or $F - X - S + R + (-)ne^- \leftrightarrow F(P) + S - X(P)$ (-)ne $^- \leftrightarrow F - X(P) + S(P)$ (2). In reaction (1), the atomic bonds between surface atoms of film F and surface atoms of substrate X break, suggesting the etching to interfacial covalent bonds between film and electrode substrate. In reaction (2), the bonds between surface atoms of substrate X and inner atoms of substrate S break, suggesting the etching to electrode substrate, where the interfacial bond F - X could be either covalent or non-covalent bond. R denote reactant electrolyte (e.g. liquid and ions), P is the function groups of reaction product, and n is the number of charge transfer in the reaction.

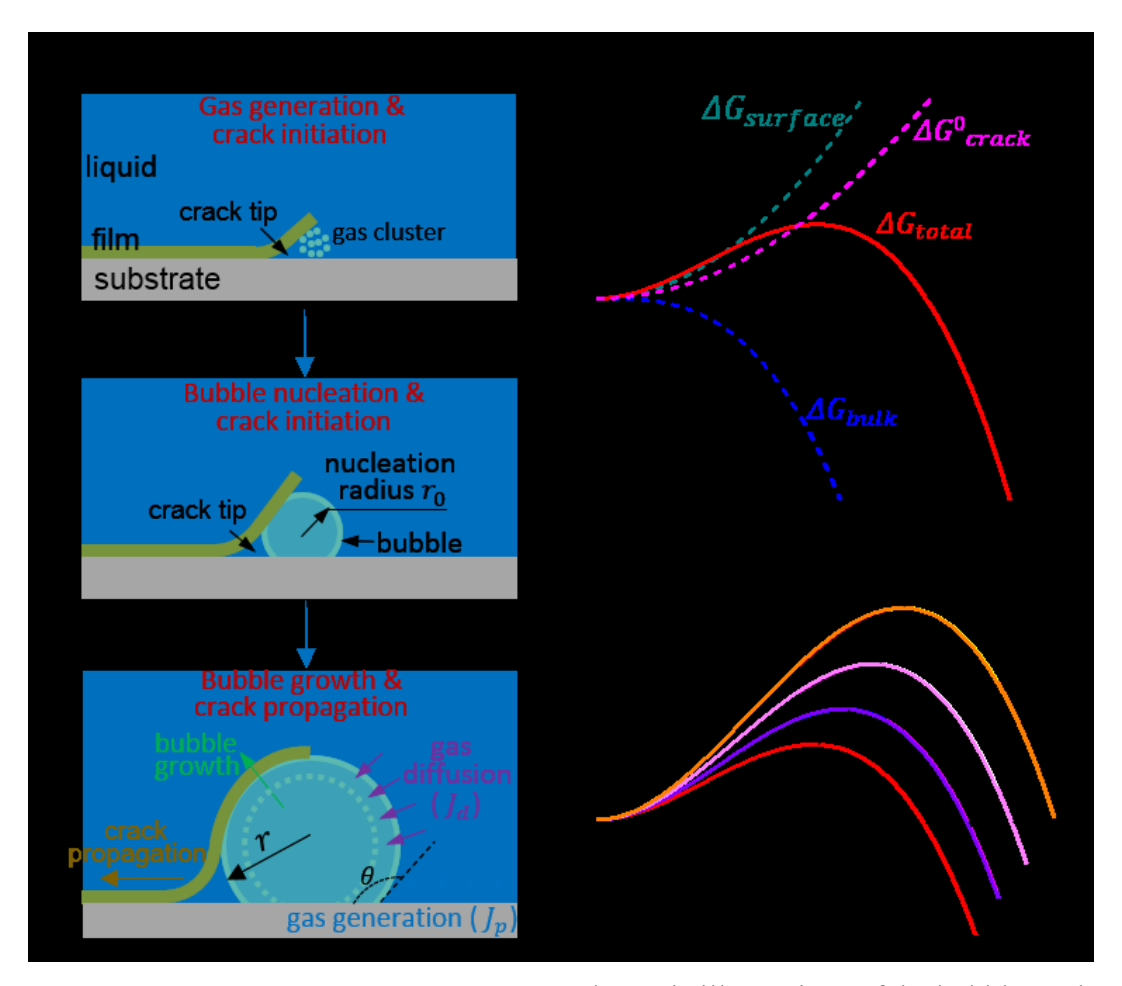


Fig. 2. Bubble transfer mechanics model. (a) Schematic illustrations of the bubble nucleation, growth and interaction with film and substrate. The gas generation and bubble nucleation leads to the initiation of crack at the interface between film and substrate (top), the growth of bubble drives the interface crack propagation (middle), and the further growth of bubble with gas diffusion along with mechanical deformation of film and its resultant interfacial crack propagation (bottom). (b) Theoretical evolution of energies as a function of bubble radius during the bubble nucleation, where G_a is the maximum total energy at the critical nucleation radius r_0 . (c) Variation of the total energy in theory as a function of bubble radius for different intrinsic interfacial adhesion energy G_0 , indicating an increased G_a with the increasing of G_0 .

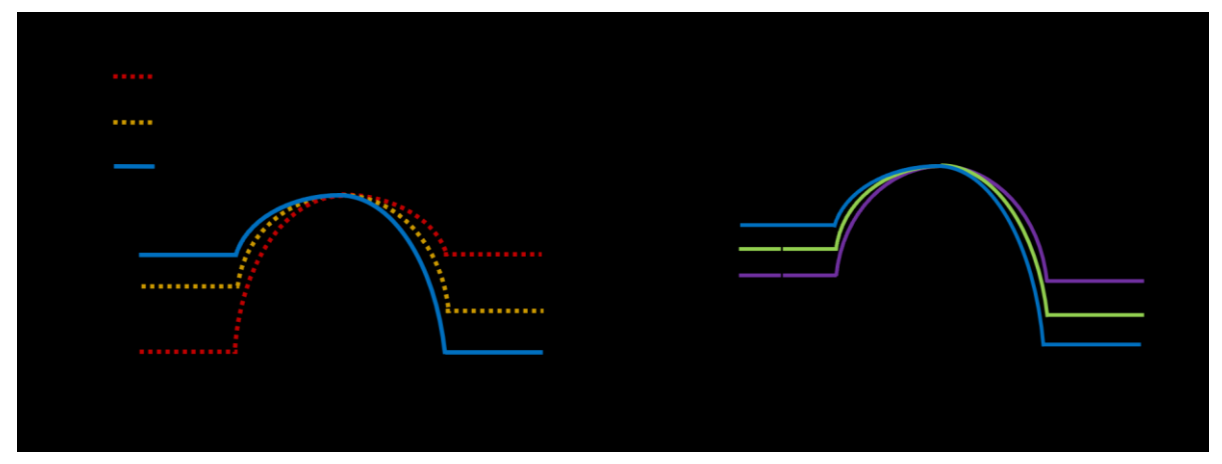


Fig. 3. Electrochemical etching transfer mechanics model. (a) Energy diagram for interfacial bond breaking by reaction without etching $F - X - S \leftrightarrow F + X - S$ (red), with chemical etching $F - X - S + R \leftrightarrow F + X(P) + S$ (yellow) and with electrochemical etching $F - X - S + R + (-)ne^- \leftrightarrow F + X(P) + S(P)$ (blue). $\overrightarrow{G_f}$ and $\overleftarrow{G_r}$ are the energy barrier for the forward bond rupture reaction and reverse bond healing reaction, respectively. (b) Energy diagram for interfacial bond breaking by the electrochemical etching reaction with variation of interfacial adhesion energy G_c and applied electrical voltage ΔU .

Table 1. Materials and system parameters used in the theoretical analysis

Description	Parameter	Value
Temperature	T	298 K
Pressure in solution	P_0	101325 Pa
Density of liquid	$ ho_l$	997 kg m ⁻³
Density of gas (H ₂)	$ ho_g$	0.081 kg m ⁻³
Density of gas (O ₂)	$ ho_g$	1.29 kg m ⁻³
Surface tension of liquid	γ_{gl}	0.072 N m ⁻¹ (Kadyk et al., 2016)
Gas transfer rate constant	k_{in}	10 ⁻⁵ m s ⁻¹ (Kadyk et al., 2016)
Saturation concentration of gas	c_{sat}	7.1·10 ⁻⁴ M (Kadyk et al., 2016)
Adhesion energy (Cu)	G_c	0.7 J m ⁻² (Xin et al., 2017)
Adhesion energy (Au)	G_c	0.25 J m ⁻² (Megra and Suk, 2019)
Conductivity of solution (NaCl)	λ	0.017 S m ² mol ⁻¹ (Widodo et al., 2018)
Conductivity of solution (KOH)	λ	0.033 S m ² mol ⁻¹ (Chen et al., 2017)
Equilibrium voltage (water electrolysis)	ΔU^0	1.23 V (Fisichella et al., 2014)
Equilibrium voltage (electrochemical etching)	ΔU^0	0.34 V (Huo, 2004)

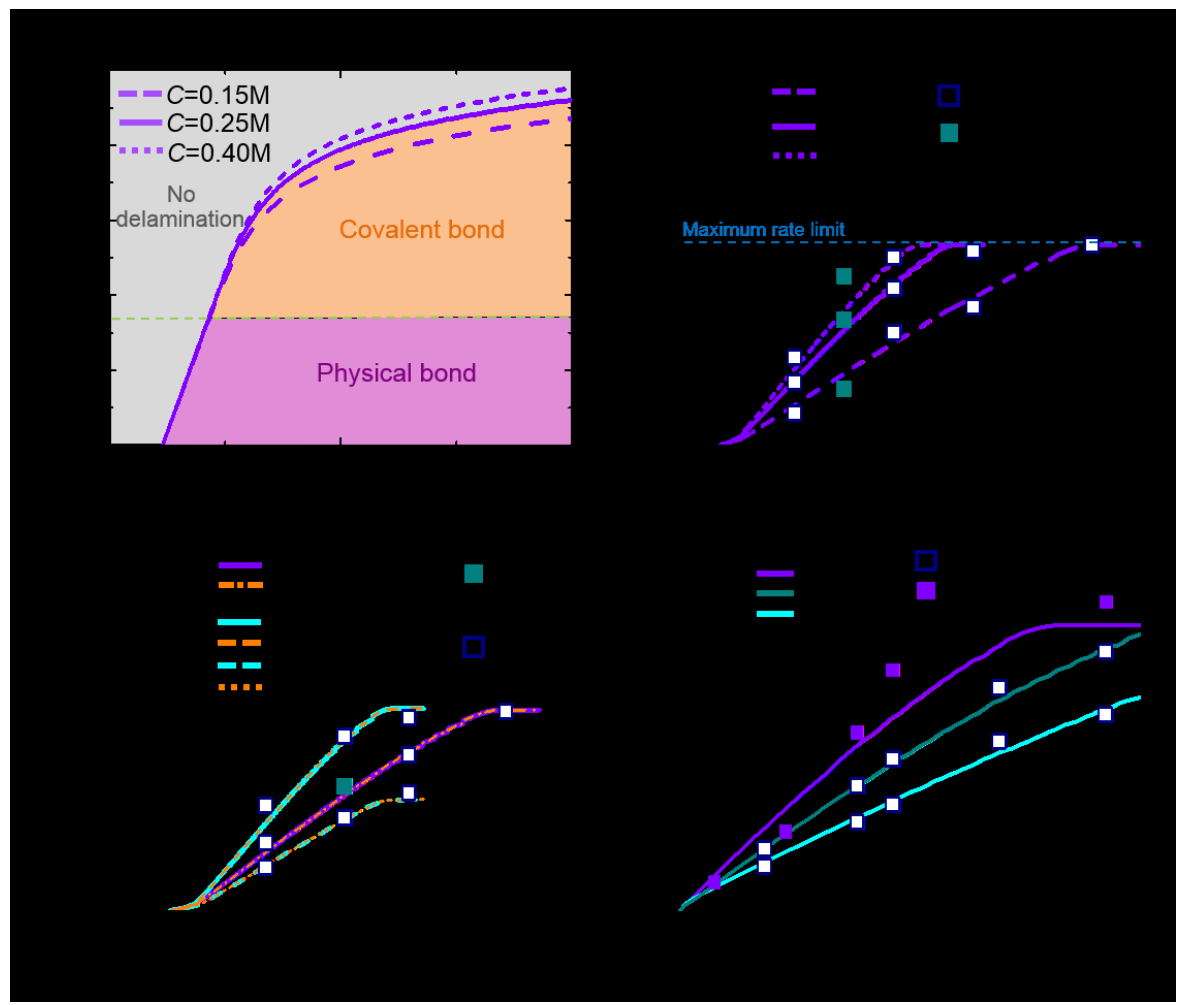


Fig. 4. Theoretical prediction and validation of interfacial delamination by bubble transfer. (a) Interfacial adhesion energy G_c as function of the critical applied electrical voltage ΔU_c that is required to delaminate the interface by bubble force mechanism under different concentrations of electrolyte C and types of interface interaction and is plotted by Equation (18) with $\overline{v}_b = 0$. The dash light green line distinguishes the G_c for interfacial bonds between film and electrode substrate with covalent or non-covalent bonds, and the gray area shows that the bubble force is not strong enough to delaminate the interface. Comparison of bubble-driven interfacial delamination rate \overline{v}_b in an applied voltage ΔU among theory, finite element (FE) simulation and experiment for a series of (b) electrolyte concentrations C, and (c) selections of electrode substrate materials, film stiffness B and electrode polarity. B=2Nnm is taken the stiffness for a PMMA film with 1 micron thickness and B=0.04uNnm is taken the stiffness for a graphene film. The maximum limit of delamination rate \overline{v}_b = \overline{v}_{bmax} is obtained at the current density limit in the reaction cell. (d) Effect of electrolyte selection on bubble-driven interfacial delamination rate \overline{v}_b .

Table 2. Comparison of the delamination rates from the proposed theoretical model and literature experiments

Delamination rate $\overline{v_b}$ in the bubble transfer

Solution concentration (M)	$\overline{\boldsymbol{v_b}}$ (mm/s)	$\overline{\boldsymbol{v_b}}$ (mm/s)
	theoretical model	experiment (Fisichella et al., 2014) ¹
0.05	0.04	0.033
0.15	0.11	0.09
0.25	0.19	0.2
0.3	0.22	0.27
0.6	0.32	0.35

^{(&}lt;sup>1</sup>The delamination experiment was performed in KOH solution with cathode of Cu, and $\Delta U = 5$ V.)

Delamination rate $\overline{v_e}$ in the electrochemical etching transfer

Electrode	$\overline{\boldsymbol{v_e}}$ (mm/s)	$\overline{\boldsymbol{v_e}} \hspace{0.1cm} (\text{mm/s})$
	theoretical model	experiments
Cu (anode)	0.021	0.017 (Shi et al., 2014) ²
Cu ₂ O (cathode)	0.16	$0.17 \text{ (Cherian et al., } 2015b)^3$

^{(&}lt;sup>2</sup>Experiment was performed in (NH₄)S₂O₈ solution (0.1M) under $\Delta U = 2$ V. ³Experiment was performed in NaCl solution (0.5M) under $\Delta U = 2.6$ V.)

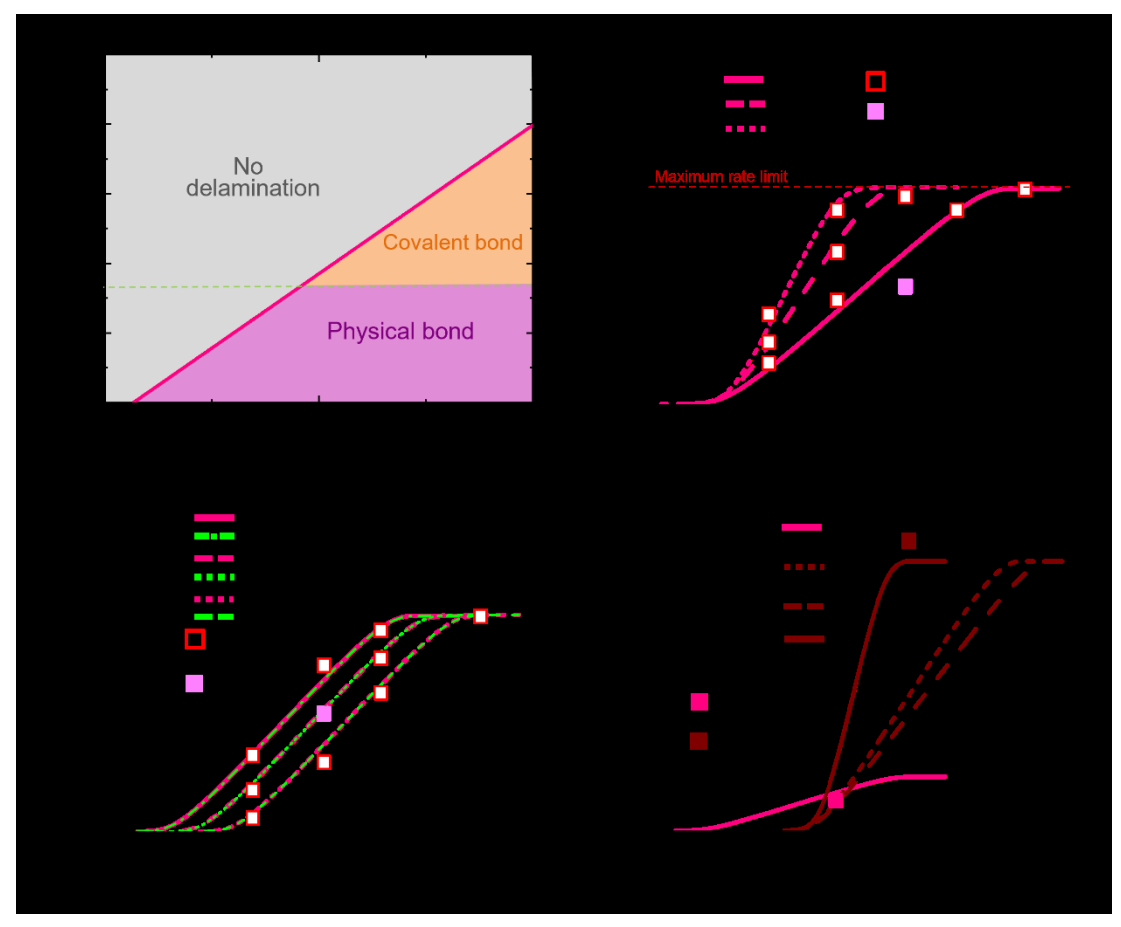


Fig. 5. Theoretical prediction and validation of interfacial delamination by electrochemical etching. (a) Theoretical relation between interfacial adhesion energy G_c and the critical applied electrical voltage ΔU_c that is required to delaminate the interface by electrochemical etching mechanism and is plotted by Equation (25) with $\bar{v}_e = 0$. The dash light green line distinguishes the G_c for interfacial bonds between film and electrode substrate with covalent or non-covalent bonds, and the gray area shows that the interface delamination will not occur by etching reaction. Comparison of electrochemical etching-driven interfacial delamination rate \bar{v}_e in an applied voltage ΔU among theory, finite element (FE) simulation and experiment for a series of (b) electrolyte concentrations C, (c) film stiffness B and interfacial adhesion energy G_c , and (d) electrode substrate materials, types of electrolyte solution, and electrolyte concentration C. B=2Nnm is taken the stiffness for a PMMA film with 1 micron thickness and B=0.2mNnm is taken the stiffness for a MoS₂ layer with 10nm thickness. The maximum limit of delamination rate $\bar{v}_e = \bar{v}_{e_{max}}$ is obtained at the current density limit in the reaction cell.

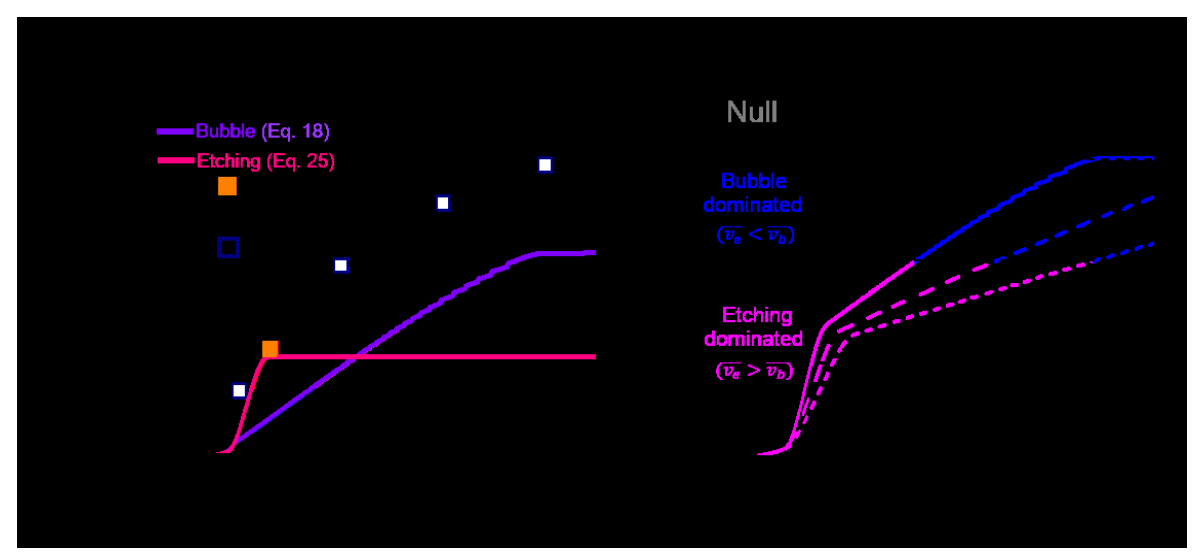


Fig. 6. Comparison of interface delamination enabled by bubble force and electrochemical etching and their coupling. (a) Interfacial delamination rate \bar{v} as a function of applied voltage ΔU enabled by bubble force, electrochemical etching and their coupled mechanisms from theory, simulation and experiment. (b) Effect of the electrolyte solution concentration C on interfacial delamination rate \bar{v} enabled by coupled delamination mechanisms. The top and bottom black dash lines denote the delamination rate at the current density limit of both electrolysis and etching reaction and $\bar{v}_e = \bar{v}_b$ of bubble force and electrochemical etching mechanism, respectively.

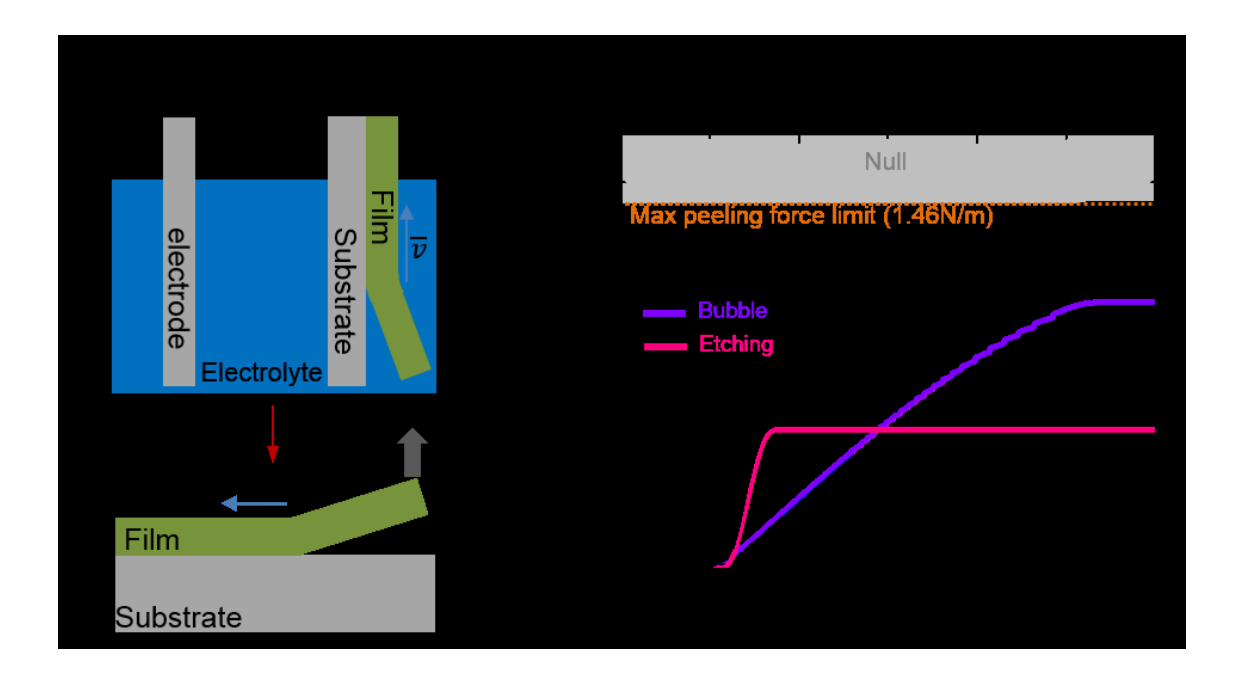


Fig. 7. Equivalent mechanical peeling model for electrochemical delamination. (a) Schematic illustrations for thin film detached from an electrode substrate enabled by electrochemical delamination at an interfacial delamination rate \bar{v} (top), and the proposed its equivalent mechanical peeling model with the hard peeling force P_e (bottom). (b) Equivalent peeling force per unit width P_e as a function of applied voltage ΔU for the electrochemical delamination mechanism by bubble force, electrochemical etching and their coupling. The detachment of film on Cu substrate is exemplified in the plots and the corresponding maximum limit of P_e is about 1.46N/m which corresponds to the maximum delamination rate \bar{v}_{max} .

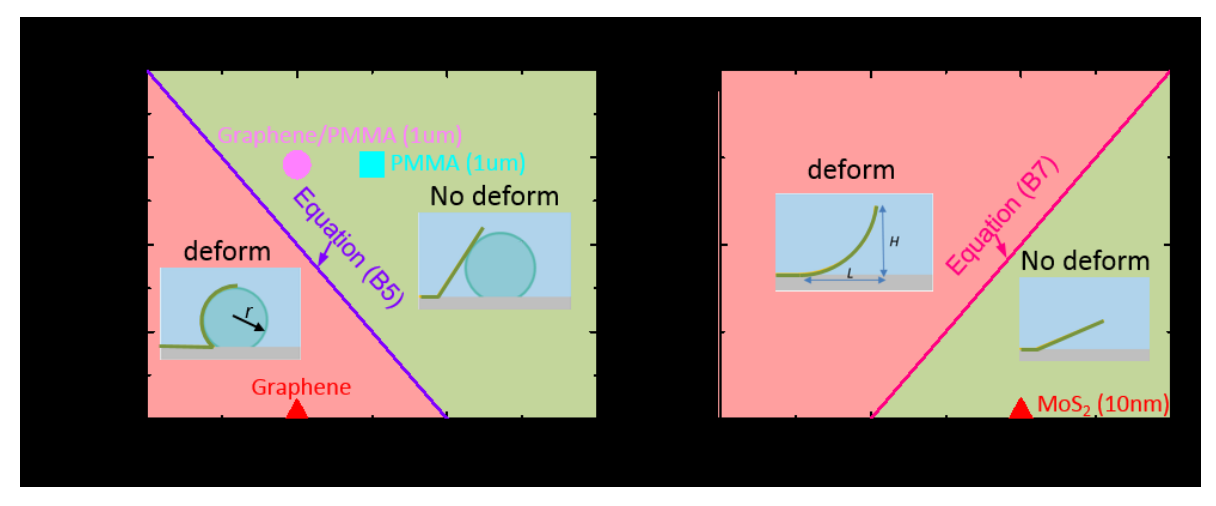


Fig. B1. Mechanical deformation of film during its delamination from electrode substrates in an electrolyte solution environment. (a) Film's deformation in the bubble transfer mechanism. With the decreasing of film modulus E and film thickness t, and increasing of liquid surface tension γ_{gl} and film/liquid contact angle θ_{fl} , the film tends to deform and wrap the bubble (left inset). By contrast, the film tends to not deform and not contact with the bubble (right inset). (b) Film's deformation in the electrochemical etching transfer mechanism. With the increasing of film modulus E, film thickness t and film/liquid contact angle θ_{fl} , and decreasing of liquid surface tension γ_{gl} , the film tends to deform (left inset). By contrast, the film tends to not deform (right inset).